

---

# Using multiple scanning angles to improve AERI thermodynamic retrievals

---

**Jongjin Seo**

A thesis submitted in partial fulfillment of

The requirements for the degree of

Master of Science

(Atmospheric and Oceanic Sciences)

at the

UNIVERSITY OF WISCONSIN-MADISON

May 2021

# Thesis Declaration and Approval

I, Jongjin Seo, declare that this Thesis titled “Using Multiple Scanning Angles to Improve AERI Thermodynamic Retrievals” and the work presented in it are my own.

<u>Jongjin Seo</u>	_____	_____
Author	Signature	Date

I hereby approve and recommend for acceptance this work in partial fulfillment of the requirements for the degree of Master of Science:

<u>Tristan L’Ecuyer</u>	_____	_____
Committee Chair	Signature	Date

<u>Grant Petty</u>	_____	_____
Faculty Member	Signature	Date

<u>Jonathan Gero</u>	_____	_____
Associate Scientist	Signature	Date

<u>Timothy J. Wagner</u>	_____	_____
Associate Researcher	Signature	Date

# Abstract

## Using Multiple Scanning Angles to Improve AERI Thermodynamic Retrievals

by Jongjin Seo

The planetary boundary layer (PBL) is the lowest part of the troposphere, which is subject to direct earth-atmosphere influence because of its proximity to the surface of the earth. Because of high variability of atmospheric properties with significant exchange of latent and sensible heat between land and atmosphere within PBL, observing thermodynamic profiles of the PBL is essential to understanding atmospheric phenomena and improvement in numerical weather prediction skill for short and medium-range forecasts.

The Atmospheric Emitted Radiance Interferometer (AERI) is a commercially available thermal infrared (IR) spectrometer used to observe the vertical structure of temperature and water vapor mixing ratio from the ground. The AERI was developed for the Atmospheric Radiation Measurement (ARM) program by the Space Science and Engineering Center (SSEC) science team at the University of Wisconsin-Madison. The AERIs are also currently deployed worldwide in various climate regimes. By its design, the AERI is limited to observing downwelling IR radiance viewed at zenith only and AERI thermodynamic retrieval algorithm has been developed to retrieve the thermodynamic state from radiances viewed at zenith. In contrast, the microwave radiometers (MWRs), operational thermodynamic profilers available from multiple vendors that observed radiance in the microwave band, have used multiple scanning angles in addition to zenith to improve retrievals. We seek to determine whether using multiple scanning angles can improve the accuracy of AERI retrievals, which has previously not been examined.

In this study, we analyze thermodynamic retrievals and information content using simulated radiances for ARM sites as well as real-world AERI-observed radiances from the ARM Cloud Aerosol Precipitation Experiment (ACAPEX) field campaign. Our results show that additional angular information increases the degree of freedom for signal for temperature and water vapor. Retrievals that use multiple scanning angles have a better root mean square of error for temperature and water vapor mixing ratio below 1 km for both the synthetic experiment and the real-world case study.

## Acknowledgments

I would first like to thank Dr. Jonathan Gero, my research advisor, for the opportunity to study at the University of Wisconsin-Madison. I never forget our first meeting looking around campus with a bicycle together at night and your cares throughout my M.S. degree. It made me feel more comfortable and friendly about living at Madison. I am also thankful for his encouragement and trust in me to work independently and all his guidance when I need them.

I would also like to thank Dr. Timothy J Wagner, my research advisor, for all his guidance and assistance on this project. He allowed me to learn the scientific backgrounds of this project as well as the AERIOe algorithm and data processing. I would like to thank Dr. David D. Turner, provided an amount of guidance and shared ideas when I got stuck. He always listened to my scientific thoughts carefully and gave great feedback.

Prof. Tristan L'Ecuyer, my academic advisor, provided excellent advice about my academic concerns and allowed me to finish the coursework and M.S. degree well. I would like to thank Prof. Grant Petty for providing great advice about my M.S. thesis. I would thank all of my peers in the AOSS for their kind.

Last, I would like to thank my parents and two sisters for always supporting me and encouraging me.

## Table of Contents

Abstract .....	i
Acknowledgments .....	ii
Table of Contents .....	iii
List of Figures .....	v
Table of Tables .....	vii
1. Introduction .....	1
2. Scientific Background .....	5
2.1 Thermodynamics of the Planetary Boundary Layer (PBL) .....	5
2.2 A Brief Review of Thermodynamic Profile Observations .....	10
2.2.1 Global Observation System (GOS) .....	10
2.2.2 In Situ Measurements .....	11
2.2.3 Spaceborne Remote Sensing Measurements .....	12
2.2.4 Ground-based Remote Sensing Measurements .....	14
2.2.4.1 Microwave Radiometer (MWR) .....	15
2.2.4.2 Atmospheric Emitted Radiance Interferometer (AERI) .....	17
2.3 Radiative Transfer in a Plane Parallel Approximation .....	20
3. Methodology .....	23
3.1 Data Resources .....	23
3.1.1 Synthetic Experiment .....	23

3.1.2 ARM Cloud Aerosol Precipitation Experiment (ACAPEX) campaign . . . . .	27
3.1.2.1 Date Selection and Cloud Filtering . . . . .	30
3.2 LBLRTM . . . . .	34
3.3 Optimal Estimation Method . . . . .	35
3.3.1 Information Content . . . . .	39
3.3.2 Scanning Angles . . . . .	40
4. Results . . . . .	42
4.1 Synthetic Experiment – Information Content . . . . .	42
4.2 Synthetic Experiment – Thermodynamic Retrievals . . . . .	51
4.3 ACAPEX Campaign – Information Content . . . . .	56
4.4 ACAPEX Campaign – Thermodynamic Retrievals . . . . .	58
5. Conclusions and Future Work . . . . .	62
5.1 Conclusions . . . . .	62
5.2 Future Work . . . . .	64
References . . . . .	66

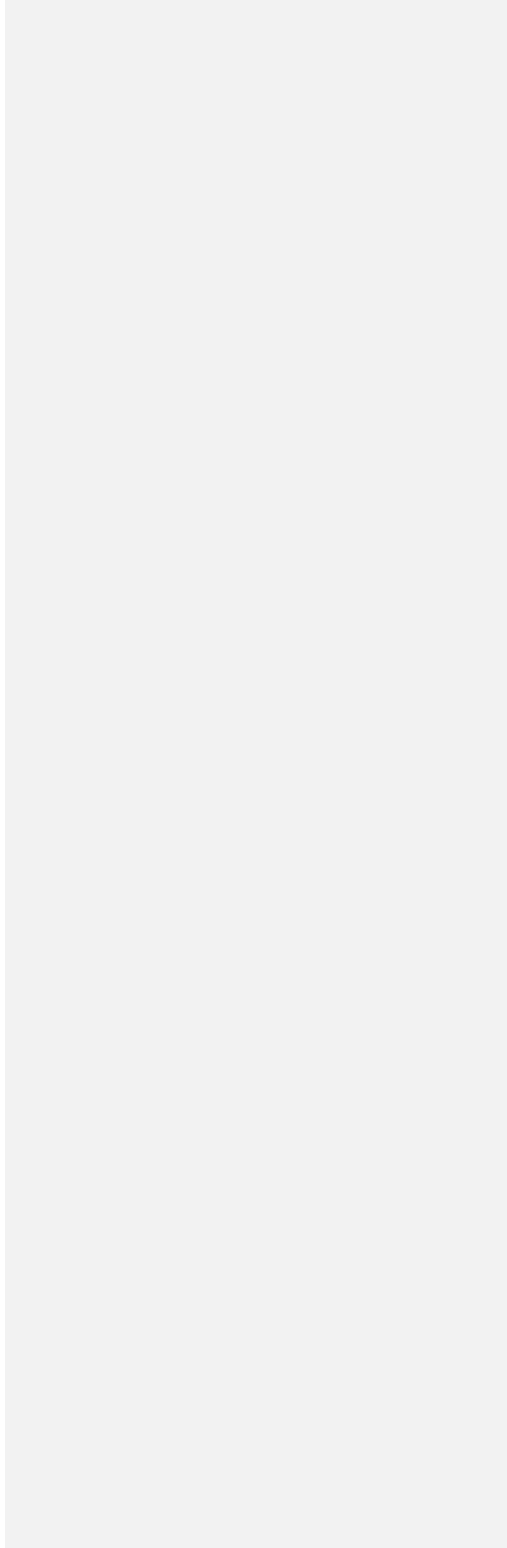
## List of Figures

2.1 Structure of the troposphere and location of planetary boundary layer . . . . .	5
2.2 The diurnal cycle of the planetary boundary layer . . . . .	7
2.3 Examples of PBL temperature profiles during the day and night over land . . . . .	9
2.4 Evolution of potential temperature $\theta$ profiles . . . . .	9
2.5 Global Observing System . . . . .	10
2.6 Map of stations with derived IGRA data . . . . .	12
2.7 Microwave Radiometer (MWR) . . . . .	15
2.8 Atmospheric Emitted Radiance Interferometer (AERI) instrument . . . . .	18
2.9 Examples of spectra measured by the M-AERI . . . . .	20
2.10 Relationship between slant and vertical paths . . . . .	22
3.1 Location of permanent ARM sites (SGP, NSA, and TWP) . . . . .	24
3.2 Mean and standard deviation of temperature and water vapor mixing ratio at ARM site in January . . . . .	26
3.3 As in 3.2, but for July . . . . .	27
3.4 Two main facilities and main observation field of ACAPEX Campaign . . . . .	29
3.5 Marine-AERI instrument deployed on a research vessel . . . . .	29
3.6 Frequency of no cloud detected from ceilometer and TSI . . . . .	31
3.7 Histogram of brightness temperature of all AERI observations in the $11\ \mu\text{m}$ between Jun 1996 and May 2010 at SGP site . . . . .	32
3.8 Standard deviation of brightness temperature (K) at the $10\ \mu\text{m}$ for zenith view . . . . .	33
3.9 As in 3.8, but for low scanning angles . . . . .	33
3.10 Degree of freedom for signal (DFS) for temperature and water vapor as a function of precipitable water vapor (PWV) . . . . .	40
4.1 Vertical structure of DFS for temperature retrieved from the ARM sites . . . . .	43

4.2 As in 4.1 but for fractional DFS	44
4.3 As in 4.1 but for DFS for water vapor	45
4.4 As in 4.3 but for fractional DFS	46
4.5 DFS of two scanning angles for temperature and water vapor retrieved from radiosonde profiles as SGP site	47
4.6 As in 4.5, but retrieved from NSA site	48
4.7 As in 4.5, but retrieved from TWP site	48
4.8 DFS of multiple scanning angles for temperature and water vapor at retrieved from radiosonde profiles at SGP site	49
4.9 As in 4.8, but retrieved from NSA site	50
4.10 As in 4.8, but retrieved from TWP site	50
4.11 AERIOe root mean square error (RMSE) for temperature (K) of two scanning angles retrieved from ARM sites	52
4.12 As in 4.11, but for water vapor mixing ratio ( $\text{g kg}^{-1}$ )	53
4.13 AERIOe root mean square error (RMSE) for temperature (K) of multiple scanning angles retrieved from ARM sites	55
4.14 As in 4.13, but water vapor mixing ratio ( $\text{g kg}^{-1}$ )	56
4.15 DFS of two scanning angles for temperature and water vapor at 4km retrieved from ACAPEX campaign	57
4.16 As in 4.15, but of multiple scanning angles	58
4.17 AERIOe root mean square error (RMSE) for temperature (K) water vapor mixing ratio ( $\text{g kg}^{-1}$ ) of two scanning angles retrieved from the ACAPEX campaign	59
4.18 As in 4.17, but of multiple scanning angles	61

## List of Tables

3.1 Location of ARM sites and period and data numbers . . . . .	25
3.2 Location of sonde stations and period for ACAPEX campaign . . . . .	37
3.3 Spectral regions used in AERIOe retrieval and the primary sensitivity . . . . .	37
3.4 Scanning angle groups . . . . .	41



# 1. Introduction

Observing the vertical structure of temperature and water vapor in the planetary boundary layer (PBL) is a crucial component for a wide range of applications, including operational situational awareness during severe weather, initialization of numerical weather prediction (NWP) models, pollution dispersion modeling, and studies of the exchange of heat and moisture between the surface and the atmosphere. The World Meteorological Organization (WMO) has managed the Global Observing System (GOS), consisting of surface observation, aircraft, ground-based and space-borne remote sensing, and weather radar observations over 60 years to provide the qualified vertical structure of temperature and water vapor information on the global scale. Additionally, the 2017 Decadal Survey highlighted the importance of thermodynamic profiles in the PBL and prioritized designing observations as an area for future investment.

One of the most well-known in-situ measurements to observe the vertical structure of temperature and humidity is the radiosonde which has the advantage of high accuracy and vertical resolution. However, the temporal and spatial resolution of the radiosonde network is limited due to the expense and labor required to launch these systems. With the development of remote sensing technologies, ground-based and space-borne instruments can complement in-situ measurements and fill in the gaps of the existing

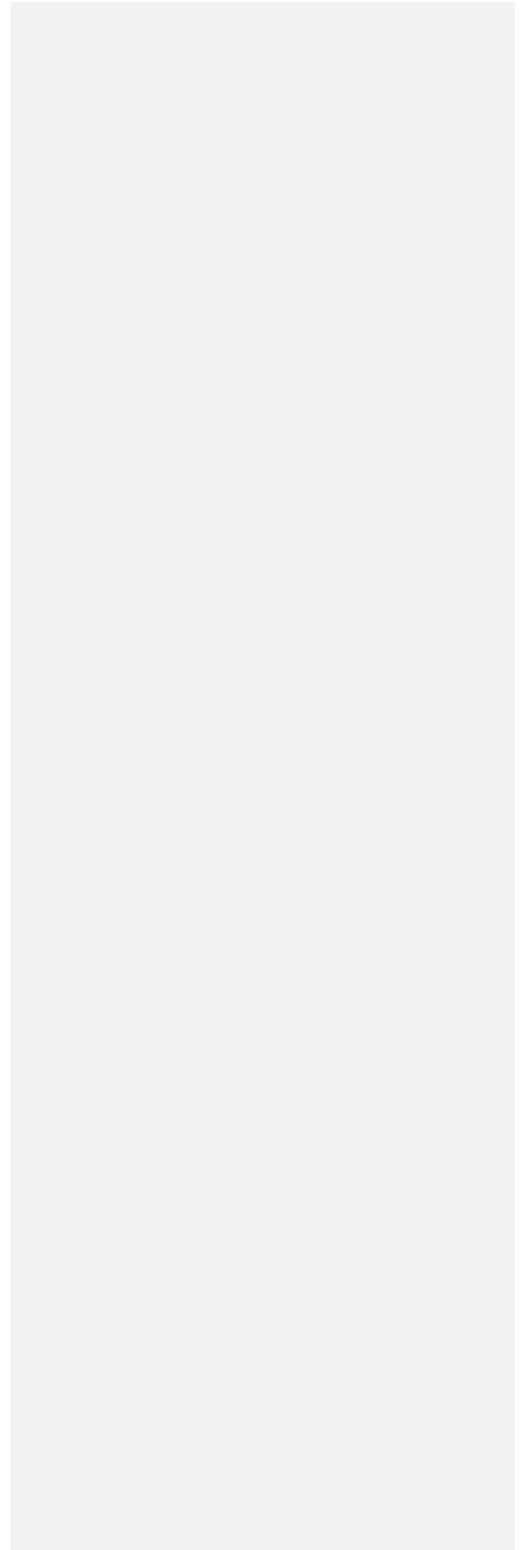
operational observing system. The satellite observations from National Aeronautics and Space Administration's (NASA) Atmospheric Infrared Sounder (AIRS) onboard Aqua (Aumann et al., 2003), Infrared Atmospheric Sounding (IASI) on the European Organization for the Exploitation of Meteorological Satellites' (EUMETSAT) Meteorological Operational (MetOp) satellites (Cayla 1993), and Cross-Track Infrared Sounder (CrIS) on Suomi-National Polar-orbiting Partnership (NPP) of the National Oceanic and Atmosphere Administration (NOAA) and NASA (Han et al., 2013) have the benefit of wide coverage on a global scale and improvement of forecast skills in global NWP (Hilton et al., 2012). However, horizontal resolution is relatively poor, and retrievals over the land surface remain very challenging with a coarse vertical resolution and accuracy of the PBL (Huang et al., 1992). Ground-based remote sensing instruments such as the Microwave Radiometer (MWR) (Löhnert et al., 2004) and the Atmospheric Emitted Radiance Interferometer (AERI) (Feltz et al., 2003) are an excellent synergistic measurement with space-borne remote sensing because of the benefit of great sensitivity near the surface and high vertical and temporal resolution. Additionally, the National Research Council (NRC) emphasized developing a national network of ground-based atmospheric profilers to fulfill the need for mesoscale monitoring and prediction in 2009.

One of the ground-based remote sensing instruments deployed worldwide in various climate conditions and fulfilled the requirements outlined by the NRC for the network is the AERI. It is a passive infrared spectrometer that observes the emitted radiance of the atmosphere. AERI observations have been used in diverse fields of atmospheric research including thermodynamic profiling, validating and improving the absorption models and spectral line parameters used in infrared radiative transfer model

(Turner et al., 2004), and retrievals of cloud properties (Turner et al., 2005), dust optical/physical properties (Turner et al., 2008), concentration of carbon monoxide (Yurganov et al., 2010) as well as long-term climate trend analyses (Gero and Turner 2011). Thermodynamic retrieval algorithms to obtain atmospheric profiles of temperature and water vapor using AERI-observed radiances have been developed, including AERIprof (Feltz et al., 1998; Smith et al., 1999) and AERIOe (Turner and Löhnert 2014; Turner and Blumberg 2018). These retrievals from AERI radiances have been used for a wide range of scientific applications including the investigation of cold fronts and drylines (Turner et al., 2000), characterizing the evolution of different convective indices in tornadic and non-tornadic storms (Wagner et al., 2008), and observing the cumulus entrainment rate retrieval scheme (Wagner et al., 2013). Because of the intrinsic instrument design, the AERI typically only observes the zenith sky, therefore the thermodynamic retrieval algorithms use only radiances of the zenith view. By contrast, the MWR community has applied multiple scanning angles to improve the accuracy in thermodynamic retrievals in the PBL since that information content and vertical resolution of retrievals from zenith is lower due to the broad weighting functions in MW (Crewell and Löhnert 2007).

In this study, we investigate the characteristics of scanning angles and the improvement to AERI retrievals using both simulated radiances and AERI-observed from a field campaign. Chapter 2 presents the scientific background of thermodynamic in the PBL and observations. In Chapter 3, the data resources, optimal estimation method, and radiative transfer model are described. Chapter 4 shows the results of information content and vertical structure for temperature and water vapor mixing ratio retrieved from

simulated radiances and AERI-observed radiances. The conclusions and future work are presented in Chapter 5.



## 2. Scientific Background

### 2.1 Thermodynamics of the Planetary Boundary Layer (PBL)

The planetary boundary layer (PBL), also known as the atmospheric boundary layer (ABL), is the lowest part of the atmosphere where we live, and its behavior is directly influenced by its contact with the surface (Figure 2.1). The PBL is mainly established by wind drag and buoyancy forces driven by the exchange of latent and sensible heat between the surface and the atmosphere. The role of the PBL is crucial in many areas including air pollution (Matthias and Bosenberg, 2002; Miao and Liu, 2019), hydrology (Pan and Mahrt, 1987), mesoscale meteorology (Pleim and Xiu, 1995), weather forecasting (Dimitrova et al., 2015) as well as climate system (Esau and Zilitinkevich, 2010).

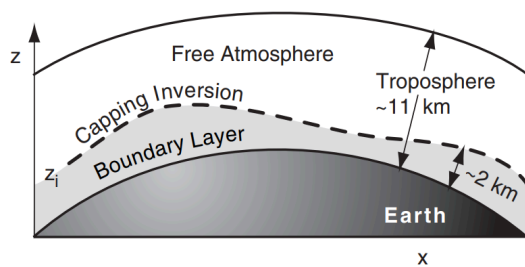


Figure 2.1 Location of the planetary boundary layer, with the top at  $z_i$  (Stull 2011).

The PBL usually responds to changes in surface radiative forcing in an hour or less. The daily cycle of radiative heating at the surface causes a diurnal cycle of the structure of the PBL (Figure 2.2). During the day, turbulence is frequent in the PBL and the physical quantities such as temperature, humidity, and pollution become homogenized so that the PBL is also called the mixed layer with vigorous turbulence. A well-mixed layer is formed when the surface is heated by the sun, and its thickness increases throughout the day. Above the PBL, free atmosphere is usually unmodified by turbulence and has a temperature profile similar to standard atmosphere. As a result of a turbulent mixed layer adjacent to the free atmosphere, there is a temperature increase at the top of PBL. This transition layer is very stable and is called the capping inversion due to acting as a cap to motions in the PBL. At night, the air temperature near the surface decreases by the radiative emission from Earth's surface. As a result, a statically stable boundary layer (SBL) forms under a neutral residual layer (RL). The RL has the moisture and pollutants from the previous mixed layer. The entrainment zone is the layer where air aloft becomes incorporated into the PBL, mixing with the fluxes of heat, moisture, and pollutants from the ground. It separates the free atmosphere from the mixed layer and is stable of intermittent turbulence.

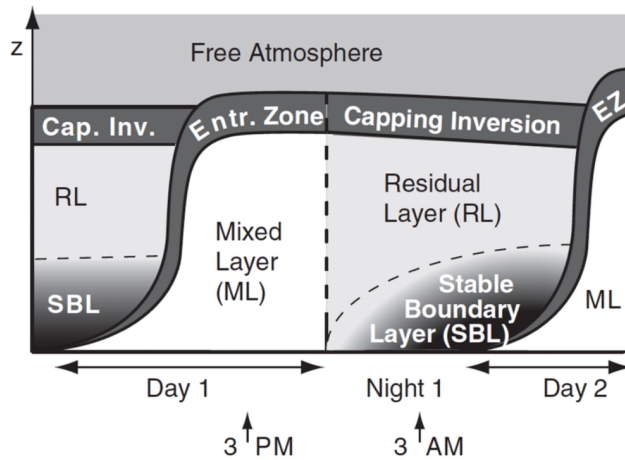


Figure 2.2 The diurnal cycle of the planetary boundary layer (Stull 2011).

On clear days, the downwelling solar radiation causes the direct heating of the surface which in turn warms the air in contact with that surface. Much of the heat absorbed by the surface is transferred to the atmosphere in a wide range of ways, including direct thermal conduction, evaporation of surface moisture, and net longwave flux. During the clear nights, heat flux from the warm air to the cold surface and radiative emission from the ground are the reasons for the cooling of atmosphere near the surface and establishing a stable PBL. The capping inversion stores heat flux and water evaporation from the surface in the PBL. It causes that heating accumulates during the day and cooling during the night within PBL. The thermodynamics of the PBL depends on the accumulated heating and cooling.

The PBL structure is reflected in the temperature profile (Figure 2.3). During the day, the environmental lapse rate in the mixed layer is close to adiabatic except for the

bottom part of the mixed layer, where a superadiabatic surface layer is found. Thermals rise from this surface layer until they arrive at the temperature inversion layer in the entrainment zone. These thermal circulations generate strong turbulence and force pollutants, potential temperature, and moisture to be well mixed in the mixed layer. At night, the bottom of the mixed layer becomes cold because of radiative cooling at the surface. This creates a stable PBL until the surface is heated by sunlight the next morning.

Seasonal variations in the evolution of the PBL are also observed (Figure 2.4). During summer at middle and high latitudes, more heating occurs during the day than cooling at night due to the longer days. The mixed layer rapidly grows through the residual layer, and it continues to rise into the free atmosphere. If the air contains sufficient moisture, cumulus clouds can form. At night, the shallow PBL near the ground becomes stable. During winter, more cooling occurs during the long nights than heating during the short days so that stable PBLs dominate, and there is a net temperature decrease over the diurnal period. Any non-frontal clouds present are typically stratiform or fog. Additionally, the thermodynamics of the PBL are directly connected to wind profile, turbulence, and convection during the day. Therefore, thermodynamics in the PBL has a critical role in understanding the atmospheric dynamics and kinematics of the lower troposphere, and observations of the vertical structure of temperature and water vapor with the high temporal and vertical resolution are essential.

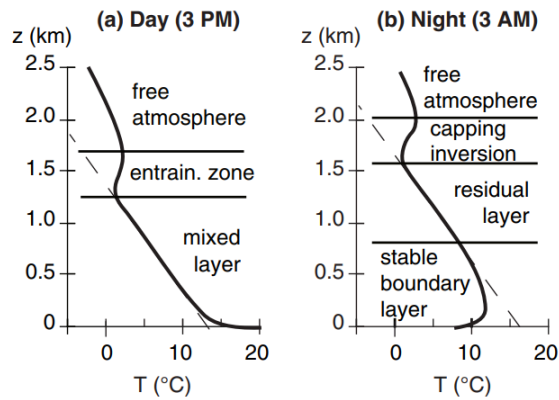


Figure 2.3 Examples of PBL temperature profiles during the day (left) and night (right) over land. The adiabatic lapse rate is dashed. In the real PBL the height can be greater or smaller, depending on location, time, and season (Stull 2011).

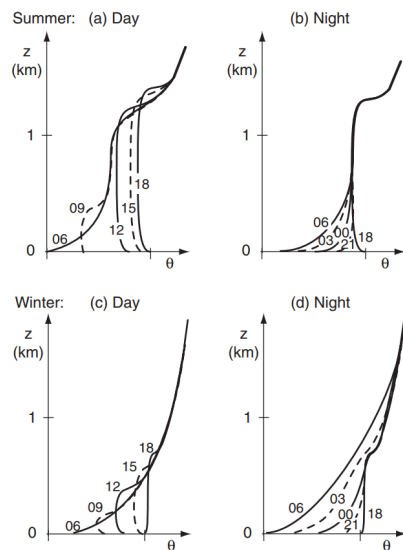


Figure 2.4 Evolution of potential temperature  $\theta$  profiles. Curves are labeled with local time in hours. (Stull 2011)

## 2.2 A brief review of thermodynamic profile observations

### 2.2.1 Global Observing System (GOS)

An example of the most ambitious and successful instances of international collaboration for providing operational atmospheric observations is the World Meteorological Organization (WMO) Global Observing System (GOS) (Figure 2.5). GOS consists of a coordinated network for acquiring meteorological and other environmental observations on a global scale, including surface stations, marine, radiosonde, airborne, ground-based and space-borne remote sensing observation, as well as other observation platforms owned and operated by a plethora of national and international agencies with different funding lines, allegiances, overall priorities and management processes: these observations are collected for both meteorological and climatological applications with a significant synergy effects. This operational network is mainly maintained by national meteorological services (NMSs) and national and international organizations such as NOAA and EUMETSAT.

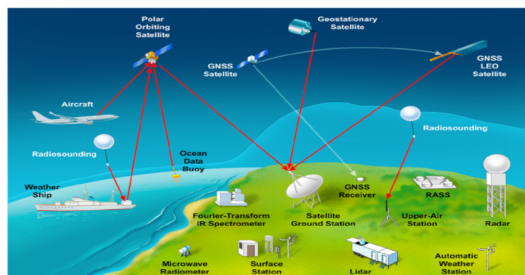


Figure 2.5 The Global Observing System (GOS) showing the synergy of in situ, passive, and active remote sensing systems for the thermodynamic profile. The shading of the atmosphere above the surface indicated the PBL layer. (Wulfmeyer et al., 2015)

Through the combination of the Global Telecommunication System (GTS), the Global Data-processing and Forecasting System (GDPFS), and GOS, billions of observations are obtained and exchanged in real-time between WMO Members and other partners every single day. Data from the GOS are used for a wide range of research projects within the Global Energy and Water Exchanges (GEWEX) Data, Assessment Panel (GDAP), and various other teams such as the Global Climate Observing System (GCOS) and NOAA's National Centers for Environmental Information (NCEI). Additionally, the long-term objectives of the GOS are to improve and optimize global observation systems for the preparation of increasingly accurate weather analysis, forecasts, and warnings, and climate and environmental monitoring activities and provide for the necessary standardization of observing techniques and practices.

### 2.2.2 In-Situ Measurements

One of the widely used in-situ measurement to observe thermodynamic profile is the radiosonde. The radiosonde is a small, expendable instrument package carried aloft by a weather balloon inflated with hydrogen or helium gas. Modern sensors on the radiosonde measure the pressure, temperature, and relative humidity with high accuracy and transmit them by radio to a ground receiver with GPS position data each second. As the radiosonde rises at about 300 meters/minute, it has an excellent vertical resolution. The Integrated Global Radiosonde Archive (IGRA) consists of radiosonde and pilot balloon observations at over 2,700 globally distributed stations (Figure 2.6). All routine radiosonde launches twice per day at the official observation time (00 UTC and 12 UTC).

It provides an instantaneous snapshot of the atmosphere. Measured and derived datasets from the radiosonde are valuable as input to air pollution models, for studies of the detailed vertical structure of the troposphere, for assessing the atmospheric conditions during particular meteorological events, for validation of remote sensing products, and for many other operational applications. The other in-situ instruments such as ships, surface stations, and buoys are used to be complimented for radiosonde data. However, they have limitations of deployment locations and field campaigns, so it is hard to derive long-term time series of thermodynamic profiles in specific regions.

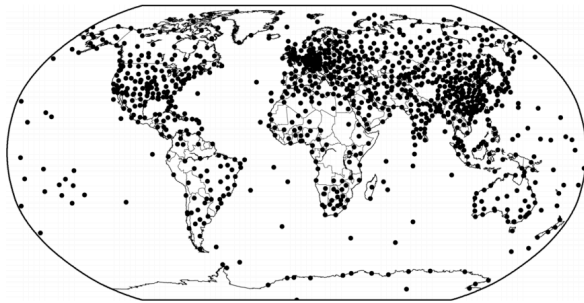


Figure 2.6 Map of the locations of stations with derived IGRA data. (Durre and Yin 2008)

### 2.2.3 Spaceborne Remote Sensing Measurements

Space-borne remote sensing measurements are usually performed in the thermal infrared (IR) and microwave (MW) spectral regions where the water vapor absorption or atmospheric emission in absorption bands is influenced by temperature to retrieve thermodynamic information. Global operational observations of water vapor and the temperature became possible with the launch of the Television Infrared Observational

Satellite program (TIROS)-N/NOAA polar-orbiting satellites in 1978 (Schwalb 1978) carrying the High-Resolution Infrared Radiation Sounder (HIRS) and Microwave Sounding Unit (MSU) instruments (Susskind 1984). Whether a considerable advance was achieved by combining IR and MW remote sensing sounders since 1978, it was consistently suggested the development to satisfy the operational high vertical resolution of thermodynamic retrievals from satellites for the future climate monitoring system (Chedin et al., 1993; Stephens 1994).

These concerns have motivated the development of more elaborated IR and MW sounding systems by using increased spectral resolution and coverage with high spectral resolution cross track scanning spectrometer. The effort leads to the launch of the MetOp platforms of EUMETSAT, NASA's Aqua and Terra satellites, and Suomi National Polar-orbiting Partnership (NPP) satellite. The sensors of these satellites are the Infrared Atmospheric Sounder Interferometer (IASI), which is a Fourier transform spectrometer with  $0.5\text{ cm}^{-1}$  resolution, the Atmospheric Infrared Sounder (AIRS), a grating spectrometer with  $0.4 - 2.0\text{ cm}^{-1}$  resolution, the Cross-track scanning Infrared Sounder (CrIs), which is Fourier transform spectrometer with  $0.625\text{ cm}^{-1}$  resolution.

For example, IASI allows a good sampling in clear and partly cloudy areas by a matrix of  $2 \times 2$  circular pixels of 12 km footprint diameter each at nadir. The measurements are taken every 50 km with a swath width of 2200 km and a twice a day global earth coverage. The vertical resolution of retrievals is driven by the width of the averaging kernels in the radiative transfer model, the spectral resolution, and the radiometric noise. In the case of infrared water vapor retrievals, this results in a vertical resolution of 2 km with an accuracy of 10% in the middle to the upper troposphere and 2

Commented [GWPI]: Units are not normally italicized

km and 20% in the lower troposphere, respectively (Pougatchev et al., 2009). The resolution of the temperature profile is somewhat higher (1 km), and the accuracy is approximately 1 K in the middle and upper troposphere degrading to 2km and 2 K in the lower troposphere (Li et., 2000, Pougatchev et al., 2009; August et al., 2012). The retrievals over the land surface remain very difficult due to a significant dependence of the surface emissivity on soil moisture and vegetation. As a result, there is research about the synergy of combined satellite and ground-based remote sensing measurements to improve thermodynamic retrievals (Ebell et al., 2013; Toporov and Löhnert 2020).

#### 2.2.4 Ground-based Remote Sensing Measurements

The advantage of in-situ and space-borne remote sensing measurements can have significant synergy effects with networks of operational passive ground-based remote sensing using IR and MW spectrometers. A ground-based passive radiometer measures the radiation emitted by the atmospheric constituents such as oxygen, water vapor, cloud droplets, and carbon dioxide. Using passive radiometry had rapidly developed within the last decade since radiometers became commercially available. The ground-based Fourier transform infrared (FTIR) spectrometer (Feltz et al., 2003) and MWR networks (Cadeddu et al., 2013) are already operating within the Atmospheric Radiation Measurement (ARM) observation sites as well as networks of MWRs that are utilized in Europe (Crewell et al., 2004) and are being combined in a global network of passive remote sensing systems called MWRnet for the assimilation into NWP models (Cimini et al., 2012). The operation of FTIRs and MWRs is also possible on shipborne platforms demonstrated during various

campaigns of the ARM. These ground-based remote sensing networks can provide valuable information on the temperature and humidity profiles of the lower troposphere.

#### 2.2.4.1 Microwave Radiometer (MWR)

The microwave radiometer (MWR) (Figure 2.7) has been designed to achieve increased accuracy in the retrieval of precipitable water vapor and cloud liquid water path. Continuous MWR measurements can be very useful for detecting mesoscale phenomena that requires very high spatial and temporal resolutions. The long-term goal of MWR is to provide the scientific community with reliable, calibrated radiometric data and retrievals with well-characterized uncertainties. MWR profilers operate at several frequencies along with the 23.335-31.4 GHz, sensitive to water vapor and cloud liquid water, and 51-58 GHz oxygen absorption, sensitive to atmospheric temperature. The instrument itself is a sensitive microwave receiver composed of a Gaussian optical antenna, a noise diode injection device, and two Gunn diode oscillators used for frequency selection. The field of view is frequency-dependent, 2° for oxygen line and going from 5.9° at the lower channel to 4.5° at the higher one for water vapor.



Figure 2.7 Microwave Radiometer (<https://www.arm.gov/capabilities/instruments/mwr>)

The retrievals from MWR networks are crucially important because of the critical role that water vapor and liquid water path play in the Earth's radiative budget (Turner et al., 2007), cloud-aerosol interaction (McComiskey et al., 2009), and the climate system in general. They have served as the reference for several ARM-sponsored water vapor studies (Revercomb et al., 2003; Mattioli et al., 2007) for comparisons of various water vapor measurement techniques involving sun photometers (Schmid et al., 2001) and the Global Positioning System (Braun et al., 2003), as well as liquid water measurement techniques (Greenwald et al., 1999). It also has been widely used by the scientific community to improve gas spectroscopy in the microwave region (Liljegren et al., 2005; Payne et al., 2008), to develop new retrievals of precipitable water vapor and liquid water path (Turner, 2007; Turner et al., 2007b), and investigation of cloud properties with long period (Del Genio and Wolf, 2000; Doran et al., 2002). The MWRs serve as the water vapor calibration reference for ARM-launched radiosondes (Turner et al., 2003) and the operational Raman lidars at the ARM observation sites (Turner and Goldsmith, 1999).

Retrieval algorithms of temperature and water vapor from the MWR were developed using the statistical regression method (Löhnert and Crewell 2003). An extensive radiosonde data set is used to generate synthetic brightness temperature using the Monochromatic Radiative Transfer Model (MonoRTM, Clough et al., 2005). A multiple linear regression between brightness temperature from MonoRTM and atmospheric temperature is derived for each height from a training data set and evaluated based on a test data set. The vertical resolution of retrievals using radiance observed zenith-only has been estimated as the half-width of the vertical interlevel covariance function of retrieval errors, which decreases rapidly from 500 m at the height of 300 m to

about 1 km at the height of 500 m (Liljegren et al., 2004). The root mean square (RMS) accuracy is about 0.6 K close to the surface and degrades to about 1.5-2 K in the middle troposphere for temperature, and 0.2-0.3  $gm^{-3}$  near the surface and 0.8-1.0  $gm^{-3}$  from 1- to 2 km altitude for water vapor (Güldner and Spänkuch 2001).

The MWR community has developed the algorithms to use multiple scanning angles to improve the retrievals in the PBL (Crewell and Löhnert 2007). The first theoretical study was performed through a multiresolution wavelength technique for different radiometer configurations, e.g., angles, channels, and bandwidths (Cadeddu et al., 2002). This simulation suggests that using multiple scanning angles is favorable for altitudes below 1km, assuming horizontal homogeneity of the atmosphere. An example of this is the microwave radiometer humidity and temperature profilers (HATPRO) that observes six scanning angles between about 5° to 90° (zenith direction). The vertical resolution of retrievals from multiple scanning angles has been estimated using the Dirac delta function to decrease from 8 m at a height of 10 m to about 300 m at a height of 400 m which is better than the vertical resolution of a single zenith. The temperature retrieval using multi-angular information is significantly improved in the lowest 2 km (Crewell and Löhnert 2007). Also, multiple scanning mode gives a better shape of the temperature profile than the single zenith mode (Massaro et al., 2015).

#### 2.2.4.2 Atmospheric Emitted Radiance Interferometer (AERI)

The Atmospheric Emitted Radiance Interferometer (AERI) (Figure 2.8) was developed for the ARM program by the Space Science and Engineering Center (SSEC) at

the University of Wisconsin-Madison and is currently deployed by ARM and other entities around the world. This FTIR instrument observes downwelling emitted infrared spectrum from 530 to 3050  $cm^{-1}$  (19.0 to 3.3  $\mu m$ ) with a spectral resolution better than one wavenumber (Knuteson et al., 2004a). Absolute radiometric calibration is better than 1% of the ambient radiation ( $3-\sigma$ ) as every observation is calibrated against two blackbodies (one at ambient air temperature; the other held at 60°C) (Knuteson et al., 2004b). The temporal resolution of the AERI radiance observations is approximately 20 s through modification since the mid-2000s (Turner et al., 2005, 2007b). The vertical resolution of the retrievals decreases in an exponential-like manner changing from 25 m at the surface to 800 m at 3 km and 2000 m at 6 km.



Figure 2.8 The Atmospheric Emitted Radiance Interferometer (AERI) instrument (<https://www.arm.gov/capabilities/instruments/aeri>)

The first thermodynamic retrieval algorithm, henceforth called AERIprof, uses the physical retrieval method to derive thermodynamic profiles from the AERI-observed radiance. The AERIprof algorithm is based upon an onion-peeling technique (Smith et al., 1999). This method is typically faster than other physical retrieval methods such as the optimal estimation approach because the method only requires that the diagonal of the

Jacobian matrix be computed (Rogers 2000). However, a significant drawback of the onion-peeling method, especially for nonlinear applications such as infrared radiative transfer inversions, is that a good first guess is required. The AERIprof algorithm uses a statistical first guess using radiosonde profiles. Often, inadequacies of the first-guess profile in the mid-troposphere would result in the algorithm either not converging or producing poor quality retrievals. Other limitations of AERIprof are that the uncertainty of the retrieved profiles is not produced by the algorithm and no profiles retrieved at all in cloudy conditions. A new physical retrieval algorithm is developed that addresses some of the limitations of the AERIprof algorithm (Turner and Lohnert 2014; Turner and Blumberg 2018). This new algorithm, henceforth called AERIOe, uses a Gauss-Newton iterative scheme in an optimal estimation approach (Rodgers 2000). A simple modification to the traditional optimal-estimation equations, which was suggested by Masiello et al. (2012), is used that allows the algorithm to be relatively insensitive to the first-guess profile will almost always lead to a solution. Furthermore, the new AERIOe algorithm is able to retrieve thermodynamic profiles in both clear and cloudy scenes as well as liquid water cloud properties. However, the retrieval algorithm only uses the radiance observed viewing zenith because of the intrinsic instrument design of AERI.

The Marine-AERI (M-AERI) is a seagoing version of the AERI developed with growing recognition about the importance in the oceanographic community of observing sea surface temperature at a variety of wavelengths. The instrumental characteristics of M-AERI are the same as AERI including spectral range and resolution, radiometric calibration, and compositions of the interferometer (Gero et al., 2015). The M-AERI is designed for viewing zenith as well as +/- 45 degrees from the horizon to permit views of

the sea surface, ice surface, and atmospheric slant views (Figure 2.9). In this study, we use the atmospheric slant views observed by M-AERI during the ARM Cloud Aerosol Precipitation Experiment (ACAPEX) campaign to improve thermodynamic retrievals.

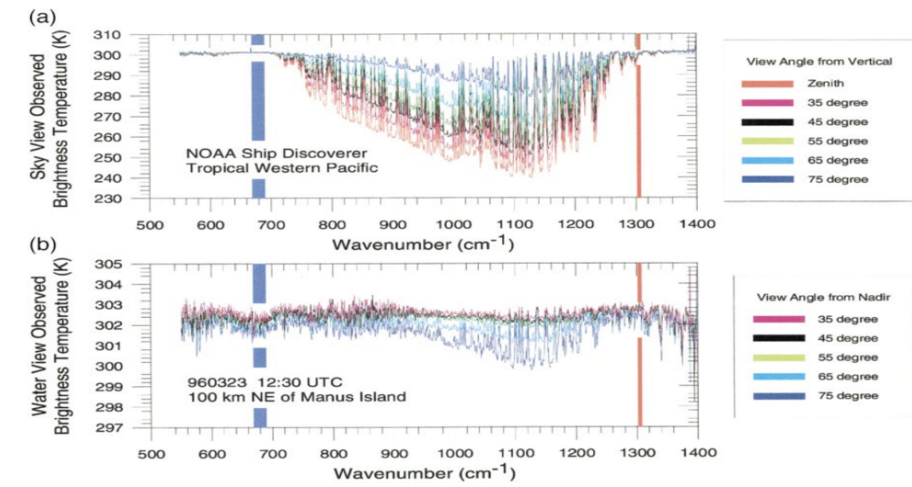


Figure 2.9 Examples of parts of spectra measured by the M-AERI while detected at the sky (top) and sea surface (bottom) at a range of angles. (Minnett et al., 2001)

## 2.3 Radiative Transfer in a Plane Parallel Atmosphere

The plane parallel approximation is usually used in the radiative transfer model, which assumes that the atmosphere is considered to be horizontally homogeneous, and properties such as pressure, density, temperature, and composition are the function of vertical direction  $z$  only (Petty 2006). The downward emitted radiation in the IR region arrived at the ground,  $I^{\downarrow}(0)$ , with the plane parallel approximation can be written as

$$I^\downarrow(0) = I^\downarrow(\infty)t^* + \int_0^\infty B[T(z)]W^\downarrow(z)dz \quad (2.1)$$

where  $z = \infty$  represents an arbitrary point beyond the top of the atmosphere. The transmittance from the surface to the top of the atmosphere  $t^*$  is defined as

$$t^* = \exp\left(-\frac{\tau^*}{\mu}\right). \quad (2.2)$$

The total optical thickness  $\tau^*$  within the atmosphere and the direction of ray propagation  $\mu$  are expressed as

$$\tau^* = \int_0^\infty \beta_e(z)dz, \text{ and} \quad (2.3)$$

$$\mu = |\cos(90^\circ - \theta)| \quad (2.4)$$

where  $\beta_e$  is the extinction coefficient.  $\theta$  is the elevation angle, henceforth called scanning angle, from the ground (Figure 2.10). For example,  $\theta$  is equal to  $0^\circ$  for the horizon, and  $90^\circ$  for the zenith view. The  $\tau^*$  is defined as not to depend on the direction of propagation  $\mu$ . Therefore,  $t^*$  is dependent on the direction of propagation  $\mu$ . For example, at the view of zenith ( $\theta = 90^\circ$ ),  $\mu$  is 1, and the transmittance has the maximum value, however, at the slant view of atmosphere ( $\theta < 90^\circ$ ),  $\mu$  is smaller than 1, and the transmittance is decreased because the radiation experiences a much longer optical path. The  $B[T(z)]$  is the Planck function for temperature at the altitude  $z$ . The weighting function  $W^\downarrow(z)$  is expressed as

$$W^{\downarrow}(z) = -\frac{dt(0,z)}{dz} = \frac{\beta_a(z)}{\mu} t(0,z) \quad (2.5)$$

where  $\beta_a(z)$  is the absorption coefficient, and  $t(0,z)$  is the transmittance between the surface and altitude  $z$ . The spectral channels become opaque at atmospheric slant view ( $\mu < 1$ ), and it leads to an increase of sensitivity to information near the surface than at zenith view.

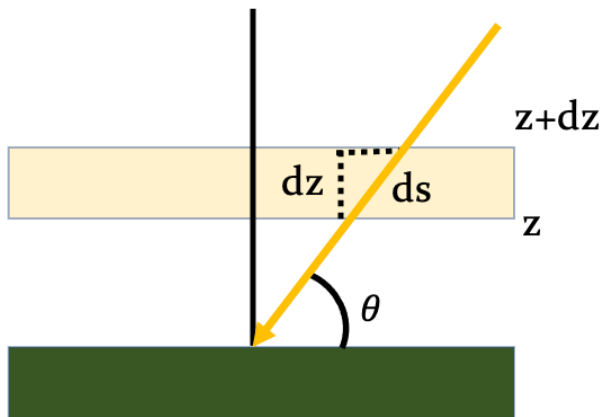


Figure 2.10 Relationship between slant and vertical paths in a plane parallel atmosphere (Petty 2006).

## 3. Methodology

### 3.1 Data resources

#### 3.1.1 Synthetic Experiment

In order to investigate the relationship between scanning angles and AERI thermodynamic retrievals, AERI radiance observations were simulated for eight scanning angles ranging from  $10^\circ$  to  $80^\circ$  and  $90^\circ$  (zenith) using a radiative transfer model and vertical structure of temperature and water vapor mixing ratio from the radiosonde profiles at three fixed ARM sites between July 2012 and December 2013 (Table 3.1). The Southern Great Plains (SGP;  $36.61^\circ\text{N}$ ,  $97.49^\circ\text{W}$ ), North Slope of Alaska (NSA;  $71.32^\circ\text{N}$ ,  $156.61^\circ\text{W}$ ), and Tropical Western Pacific (TWP;  $2.06^\circ\text{S}$ ,  $147.43^\circ\text{E}$ ) represent the broad range of climate conditions around the world (Figure 3.1). Moreover, the ARM user facility provides plenty of information with continuous and long period observations of the thermodynamic profile, cloud, and aerosol properties over a significant period of time so that it is good at doing simulation test.

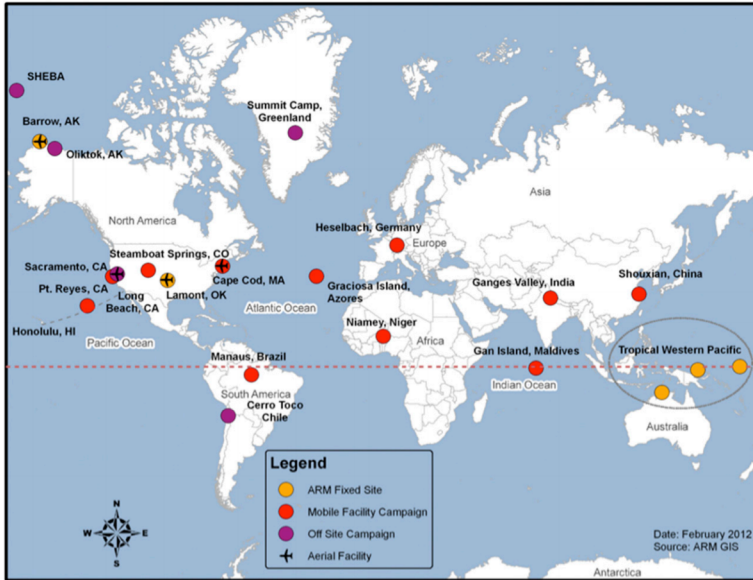


Figure 3.1 Location of the permanent ARM sites (Ackerman 2016): Southern Great Plains (SGP, Lamont, OK), North Slope of Alaska (NSA, Barrow, AK), and Tropical Western Pacific (TWP)

We used radiosonde profiles longer than 10 years at each ARM site to make a climatological thermodynamic profile (Table 3.1). The monthly mean and standard deviation of temperature and water vapor mixing ratio profiles are derived from radiosonde profiles. Figure 3.2 and Figure 3.3 are the examples in January and July. The mean temperature and water vapor mixing ratio near the ground at NSA, located in a polar climate, is less than  $-20^{\circ}\text{C}$  and  $1\text{ g/kg}$  in winter and  $2^{\circ}\text{C}$  and  $5\text{ g/kg}$  in summer so that NSA represents the atmospheric conditions that are very cold and dry in both winter and summer. In contrast, TWP, located near the equator, has a high temperature and water vapor mixing ratio near the surface throughout the year. The mean water vapor mixing

ratio is greater than 17 g/kg. The SGP, where is located in the middle latitudes, has a mean temperature and water vapor mixing ratio between NSA and TWP. Comparing the results between ARM sites is useful to understand the sensitivity of AERI thermodynamic retrievals depending on climate conditions.

Table 3.1 The location of ARM sites and period and number of radiosonde profiles to make monthly mean and standard deviation of temperature and water vapor mixing ratio and to simulate radiances for case study.

ARM Sites	Location	Type	Period	Number of radiosonde profiles
Southern Great Plains (SGP)	36.61 N, 97.49 W	Prior	2001.04.01 – 2020.12.31	27894
		Test case	2012.07.24 – 2014.01.18	144
North Slope of Alaska (NSA)	71.32 N, 156.61 W	Prior	2002.04.28 – 2020.12.31	11922
		Test case	2012.07.12 – 2014.01.14	144
Tropical Western Pacific (TWP)	2.06 N, 147.43 E	Prior	2001.04.03 – 2014.07.07	9559
		Test case	2012.08.05 – 2013.11.23	139

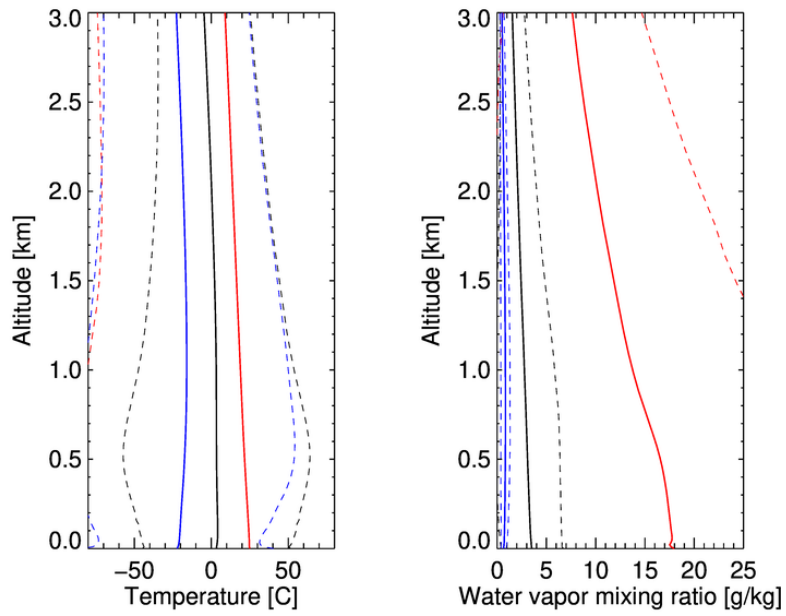


Figure 3.2 The mean (solid) and  $\pm 1$  standard deviation from mean (dashed) of temperature (left) and water vapor mixing ratio (right) from radiosonde profiles at SGP (black), NSA (blue), and TWP (red) ARM sites in January.

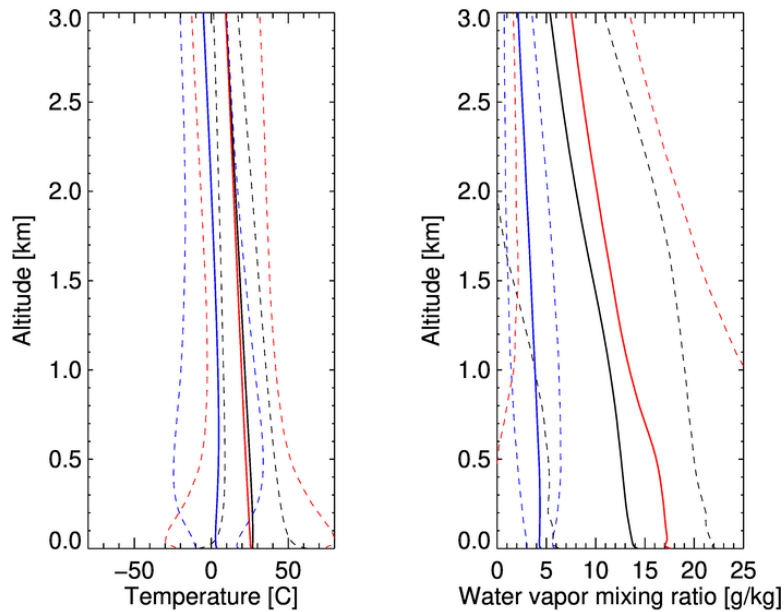


Figure 3.3 As in Figure 3.2, but for July.

### 3.1.2 ARM Cloud Aerosol Precipitation Experiment (ACAPEX)

#### Campaign

The western United States experiences precipitation predominantly during the cold season when storms approach from the Pacific Ocean, which provides about 70 – 90 percent of the water supply for the region during winter storms (Higgins et al., 2000). Understanding and modeling the fundamental processes that govern the large precipitation variability and extremes in the western U.S. is crucial for the improvement of climate models to predict the regional water cycle, including floods and droughts. One

of the most significant elements in predicting precipitation variability in the western U.S is the atmospheric rivers (ARs) which are narrow bands of enhanced water vapor associated with the warm sector of extratropical cyclones over the Pacific and Atlantic oceans. Because of the large lower-tropospheric water vapor content, strong atmospheric winds, and neutral moist static stability, some ARs can produce heavy precipitation by orographic enhancement during landfall on the U.S. West Coast (Rutz et al., 2014). The other critical element is aerosol effects on precipitation formation (for both rain and snow) because much of the rest of the orographic precipitation occurs in post-frontal clouds, which are typically relatively shallow (Rosenfeld and Givati, 2006). The ARM Cloud Aerosol Precipitation Experiment (ACAPEX) was designed to improve understanding and modeling of large scale dynamics and cloud and precipitation processes associated with ARs and aerosol-cloud interactions.

The ACAPEX campaign consisted of two main facilities to observe the atmospheric properties in the western U.S. (Figure 3.4). The first is the ARM Aerial Facility (AAF) Gulfstream-1 aircraft which was operated to probe the clouds that form over the ocean and their transformations needed for comparing the simulated and observed processes of the vertical profiles of cloud microstructure and the resultant precipitation initiation and glaciation (Fairall et al., 2018). The other is the ARM Mobile Facility (AMF2), which was deployed on a research vessel and provided critical measurements to quantify the moisture budget and cloud and precipitation processes over the Pacific. The AMF2 operated from 12 Jan 2015 to 12 Feb 2015. M-AERI was operated at the AMF2 and observed the sea surface, atmospheric slant, and zenith views (Figure 3.5). The dwell period is composed of three sea surface views, four scanning angles of 20°, 25°, 30°, and

35°, and eight zenith views (90°). The dwell period is approximately 4 min. In this study, we use the M-AERI observed radiances at four scanning angles and zenith after removing cloud samples.

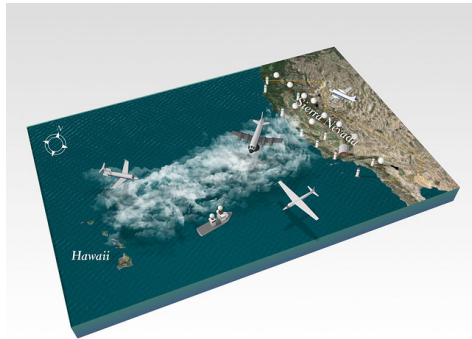


Figure 3.4 Two main facilities; 1) ARM Mobile Facility (AMF2) and 2) ARM Aerial Facility (AAF) Gulfstream-1 aircraft, and main observation field; western U.S. (<https://www.flickr.com/photos/armgov/15585313244/in/album-72157647477310974/>)



Figure 3.5 The M-AERI instrument deployed on a research vessel during the ACAPEX campaign. (<https://www.flickr.com/photos/armgov/37907508371/in/album-72157647477310974/>)

### 3.1.2.1 Date Selection and Cloud filtering

The ACAPEX campaign was conducted to study predominant precipitation processes during winter storms so that most of the days were all overcast. To find a clear day during the campaign period, we use two instruments deployed in AMF2. One is the Vaisala Laser Ceilometer, henceforth called ceilometer, which is an active remote-sensing instrument that measures cloud height, vertical visibility, and potential backscatter signals by aerosols. The laser ceilometer transmits near-infrared (910 nm) pulses of light, and the receiver detects the light backscattered by clouds and precipitation. The ceilometer has a maximum vertical range of 7700 m with a 10-m vertical resolution and a temporal resolution of 16 s. We calculate the frequency of no cloud base detected during a day (Figure 3.6). The frequencies of no cloud base detected are low at middle of the campaign period and high at the beginning and end of the campaign. The other instrument is the Total Sky Imager (TSI) which measures the fraction of the sky view covered by clouds. The TSI captures photographs of the sky dome during the daylight hours and uses digital image processing techniques to retrieve the cloud fraction for periods when the solar elevation is greater than  $10^\circ$ . The sky is considered as the clear sky if cloud cover is less than 10% (Figure 3.6). From ceilometer and TSI, we determined the 28 Jan, 09 Feb, and 10 Feb 2015 for a case study date.

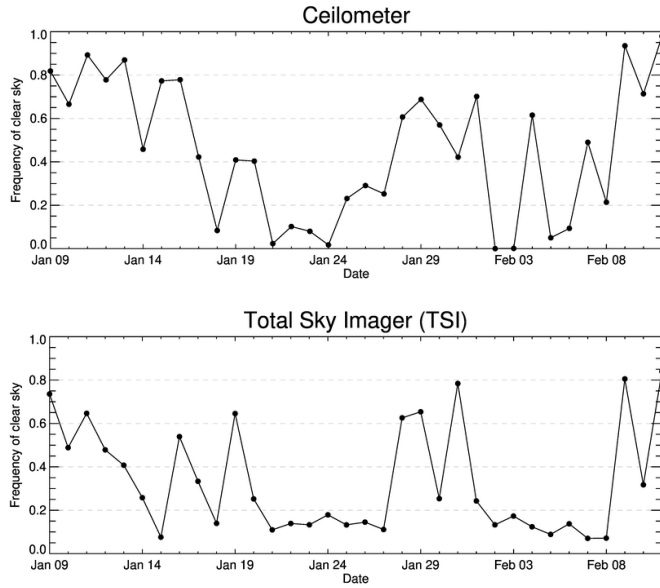


Figure 3.6 Frequency of no cloud base detected from ceilometer (top) and frequency of data that cloud cover is less than 10% from TSI (bottom).

In order to remove individual cloud samples, we use the standard deviation of brightness temperature (BT) observed from M-AERI during the field campaign. The BT at given radiance  $I_\lambda$  and wavelength  $\lambda$  can be expressed as:

$$BT = \frac{hc}{k\lambda} \ln^{-1} \left( 1 + \frac{2hc^2}{I_\lambda \lambda^5} \right) \quad (3.1)$$

where  $h$  is Planck's constant,  $c$  is the speed of light, and  $k$  is Boltzmann's constant. The BT at  $10 \mu m$  ( $985\text{-}990 \text{ cm}^{-1}$ ), where it is known as the atmospheric window, is sensitive to

clouds as the gases of the atmosphere experience very little absorption or emission at that wavelength (Figure 3.7). Figure 3.8 shows the standard deviation of BT of zenith view, and the BTs are grouped at two regions. One is where BT is less than 220 K, and it is considered as a clear sky. The other is where BT is larger than 270 K, and it is considered as a cloudy sky. Figure 3.9 shows the standard deviation of BTs at the non-zenith angles, and it is clear that these quantities have a scanning-angle dependence due to the angular dependence of optical path. The radiances associated with  $10\ \mu\text{m}$  BTs are less than 230 K were declared to be clear sky and used to retrieve thermodynamic profiles, and 62 profiles in 3 days were retrieved for the ACAPEX Campaign.

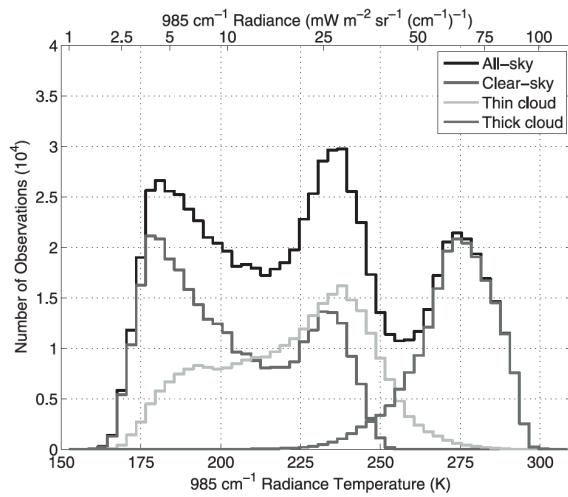


Figure 3.7 Histogram of brightness temperature (K) of all AERI observations observed at zenith view in the  $985\ \text{cm}^{-1}$  ( $10\ \mu\text{m}$ ) between Jun 1996 and May 2010 at the SGP site. Data classified as clear-sky, thin cloud, and thick cloud scenes are shown. (Gero and Turner 2015)

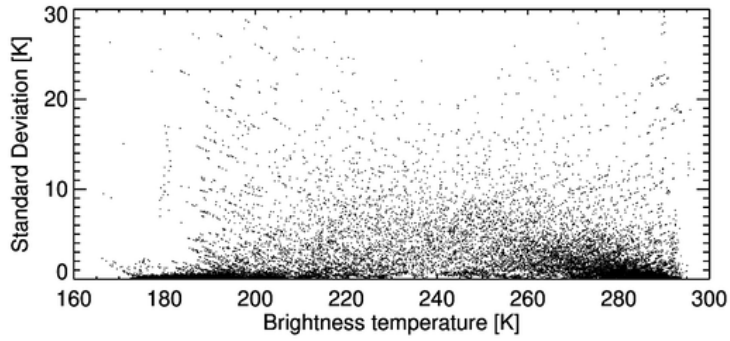


Figure 3.8 Standard deviation of brightness temperature (K) at the  $10 \mu\text{m}$  ( $985\text{--}990 \text{ cm}^{-1}$ ) of zenith view.

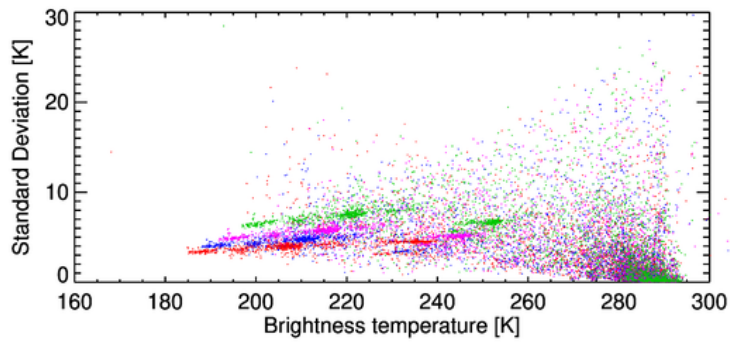


Figure 3.9 Standard deviation of brightness temperature (K) at the  $10 \mu\text{m}$  ( $985\text{--}990 \text{ cm}^{-1}$ ) for non-zenith angles; 20°(Green), 25°(Magenta), 30°(Blue), 35°(Red)

### 3.2 LBLRTM

The Line-by-Line Radiative Transfer Model (LBLRTM, Clough et al., 2005) is a well-validated model developed at the Atmospheric and Environmental Research (AER). The LBLRTM calculates the optical depth of an atmospheric layer at a given wavenumber  $\nu$  by adding the nearby absorption lines' contributions. The monochromatic optical depth for a vertical path  $\Delta z$  is given as

$$\tau_\nu = \Delta z \times [\sum_i \{ \sum_j S_{ji} f(\nu - \nu_{ji}^0) \} n_i + \sigma_\nu^{cont} n_{cont}] \quad (3.2)$$

where  $S_{ji}$  is the line intensity of the  $j$ th line of the  $i$ th atmospheric species,  $f(\nu - \nu_{ji}^0)$  is the line broadening located at  $\nu_{ji}^0$ ,  $n$  is the number density of the  $i$ th species, and  $\sigma_\nu^{cont} n_{cont}$  is the contribution of the continuum spectra. Optical properties of gases in LBLRTM use the HITRAN 2012 database (Rothman et al., 2013), and MT\_CKD 2.5 is used for the water vapor continuum (Clough et al., 2005). The Voigt profile is used for line broadening throughout the vertical range (Wells, 1999). The AERI retrieval vertical grid, ranging from surface to 17 km with spacing increasing approximately exponentially with height, is used as the vertical grid for the radiative transfer calculations. By assuming a clear sky and horizontal homogeneity of the atmosphere, the radiation systematically originates from the higher altitudes with the higher elevation angle is. This is in agreement with the fact that the atmospheric slant views yield more information about the lower atmospheric layers.

### 3.3 Optimal Estimation Method

Remote sensing instruments do not directly observe desired variables like temperature and water vapor. Rather, they observe the electromagnetic spectrum associated with a given atmospheric state from which the desired variable needs to be retrieved. The IR radiation measured by the sensor is a function of absorption and emission by elements in the atmosphere, like water vapor and carbon dioxide. This is an inverse problem, in which a mathematical technique is required to retrieve desired parameters from the observed radiance. Gauss-Newton Optimal Estimation (GNOE) is one such method for inverting radiance observations, and it is the heart of the AERIOe retrieval algorithm. It is well known for its capability in moderately nonlinear problems as well as its ability to propagate model and measurement error throughout the inversion. GNOE uses Bayesian statistics to find a solution by using the maximum likelihood method and assumption that the error covariances have Gaussian probability distribution functions from the mean state vector (Rodgers 2000). The optimal estimation equation used in the AERIOe algorithm is as follows (Rodgers 2000; Turner and Blumberg 2018):

$$X^{n+1} = X^n + [(1 + \gamma)S_a^{-1} + K_n^T S_\epsilon^{-1} K_n]^{-1} [K_n^T S_\epsilon^{-1} (Y - F(X^n)) - S_a^{-1} (X^n - X_a)] \quad (3.3)$$

where superscripts T and  $-1$  are the matrix transpose and inverse respectively. The state vector  $X$  is the vertical structure of the temperature and water vapor mixing ratio. An *a priori* of the state vector  $X_a$  and error covariance matrix  $S_a$  is calculated from the mean and covariance of a radiosonde data set. The prior profiles for ARM sites were made using

10 - 20 years of radiosonde profiles at the SGP, NSA, and TWP sites to represent various climate conditions. The prior profile for the ACAPEX campaign was made using 10 years of radiosonde profiles operated at Oakland (37.73°N, 122.21°W) and San Diego (32.85°N, 117.12°W), CA (Table 3.2). The Jacobian matrix  $K_n$  is defined as:

$$K_n = \frac{\partial F(X^n)}{\partial X^n} \quad (3.4)$$

where  $F(X^n)$  is the computed radiance using LBLRTM and the state vector  $X^n$ .  $Y$  is the AERI-observed radiance. The spectral regions used in the algorithm consist of three carbon dioxide absorption bands for temperature and one water vapor absorption band (Table 3.3). The error covariance of the observation  $S_e$  is computed from the spectral standard deviation of the calibrated imaginary radiance spectrum (Knuteson et al., 2004b). The matrix of  $S_e$  is assumed to be diagonal with no significant off-diagonal elements because the calibration of each of the over 5000 spectral elements in the AERI data is determined independently from each other, thus there are no intra-channel correlations. To count for unexpected uncertainties such as very thin clouds, movement of the ship, and the horizontal inhomogeneity of the atmosphere,  $S_e$  is doubled for observed radiances during the ACAPEX campaign. The  $\gamma$  is the Levenberg Parameter and serves as damping factor to change the relative weight between the observations and the prior information to the solution, with values of  $\gamma > 1$  corresponding to less information from the observation relative to the prior. The fixed sequence of  $\gamma$  values as a function of iteration – 1000, 300, 100, 30, 10, 3, 1, 1, 1, ... – are determined by empirical experiments (Turner et

al., 2014) and it allows more information from the observation to be used in each iteration. This is useful to stabilize the retrieval and overcome a poor first guess.

Table 3.2 The location of sonde stations and period and number of radiosonde profiles to make mean and standard deviation of temperature and water vapor mixing ratio.

Sonde stations	Location	Period	Number of radiosonde profiles
San Diego, CA	32.86 N, 117.12 W	2006.01.01 – 2016.12.31	7893
Oakland, CA	37.73 N, 122.21 W	2006.01.01 – 2016.12.31	7895

Table 3.3 Spectral regions used in AERIOe retrieval, and the primary sensitivity of each spectral region. After Turner and Blumberg (2018)

Primary Sensitivity	Starting wavenumber ( $cm^{-1}$ )	Ending wavenumber ( $cm^{-1}$ )
Temperature	612.0	618.0
	624.0	660.0
	674.0	713.0
Water vapor	538.0	588.0

The convergence is determined by the equation at each step which is given by

$$(X^n - X^{n+1})^T S^{-1} (X^n - X^{n+1}) \ll N \quad (3.5)$$

where  $N$  is the dimension of the state vector, the  $S$  is the posterior error covariance matrix that allows the sensitivity of the forward model and the uncertainties in both the prior and the observations to be propagated into the uncertainty of the solution. It can be calculated as

$$S = B^{-1} (\gamma^2 S_a^{-1} + K_n^T S_\epsilon^{-1} K_n) B^{-1}, \quad (3.6)$$

where  $B$  is as follows:

$$B = (\gamma S_a^{-1} + K_n^T S_\epsilon^{-1} K_n). \quad (3.7)$$

This compares the difference in the retrieved variables from the current iteration to the previous one. If the change in the retrieved state vector is substantially less than the magnitude of the error associated with the retrieval, then it is assumed that the retrieval has converged within its own error bars, and additional iterations would bring no additional information. The iterations can also be stopped when  $RMS_{n+1} > \gamma_n RMS_n$  or a set the upper limit on the number of iterations has been reached.

### 3.3.1 Information Content

To determine the sensitivity of each scanning angle to change in thermodynamic retrievals, we analyze the degree of freedom for signal (DFS), one of the quantities to describe information content (IC), at the convergence state. The DFS represents the number of independent pieces of information from the observation used in the solution and is calculated from the trace of the averaging kernel matrix  $A$ :

$$A = B^{-1}K_n^T S_\epsilon^{-1} K_n. \quad (3.8)$$

To study variations of DFS with height and different scanning angles, we will investigate the vertical structure of DFS and total DFS at 4 km. Previous work (Turner and Löhnert 2014) has found that the DFS for water vapor is strongly dependent on atmospheric humidity state such as precipitable water vapor (PWV) (Figure 3.10). The DFS is decreasing as PWV increases because some spectral regions used in the retrieval become opaque when PWV is high. We will investigate this relationship in synthetic experiments for different climate conditions.

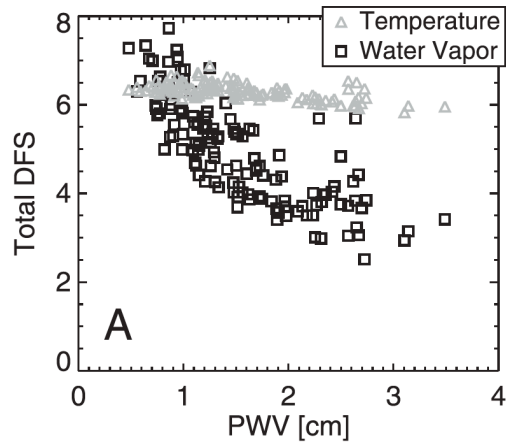


Figure 3.10 Degree of freedom for signal (DFS) for temperature and water vapor as a function of precipitable water vapor (PWV) (Turner et al., 2014)

### 3.3.2 Scanning Angles

To study the effects of different scanning angles on thermodynamic retrievals, we use two angle group sets: 1) one set that consists of two scanning angles: zenith and one more other scanning angle ranging from  $10^\circ$  to  $80^\circ$ , 2) another set that consists of zenith and other angles in which the set is expanded as additional scanning angles from low to high are included (Table 3.4). From the first set, we study how a non-zenith angle impacts the retrieval. Through the study of the second set, we are looking at the effects of numbers of scanning angles to change on DFS and the vertical structure of temperature and water vapor mixing ratio. The results are compared with zenith-only.

Table 3.4 Two group sets 1) Two scanning angles set, 2) Multiple scanning angles set

	Two Scanning angles set	Multiple Scanning angles set
Synthetic Experiment	$10^\circ+90^\circ$ , $20^\circ+90^\circ$ , $30^\circ+90^\circ$ , $40^\circ+90^\circ$ , $50^\circ+90^\circ$ , $60^\circ+90^\circ$ , $70^\circ+90^\circ$ , $80^\circ+90^\circ$	$10^\circ+90^\circ$ $10^\circ+20^\circ+90^\circ$ $10^\circ+20^\circ+30^\circ+90^\circ$ $\vdots$ $10^\circ+20^\circ+\dots+70^\circ+90^\circ$ $10^\circ+20^\circ+\dots+70^\circ+80^\circ+90^\circ$
ACAPEX Campaign	$20^\circ+90^\circ$ , $25^\circ+90^\circ$ , $30^\circ+90^\circ$ , $35^\circ+90^\circ$	$20^\circ+90^\circ$ $20^\circ+25^\circ+90^\circ$ $20^\circ+25^\circ+30^\circ+90^\circ$ $20^\circ+25^\circ+30^\circ+35^\circ+90^\circ$

## 4. Results

### 4.1 Synthetic Experiment – Information Content

The DFS for temperature and water vapor are calculated from retrievals at SGP, NSA, and TWP. Figure 4.1 shows the mean vertical structure of DFS for the temperature of the two scanning angles set. The additional DFS for temperature is decreasing in an exponential-like manner due to the strong absorption of carbon dioxide near the surface. The spectral channels used for temperature in the AERIOe algorithm become opaque and contain little additional information at high altitudes. Zenith +10° shows the largest DFS gain compared with all the other angles, at all sites. This means that the low scanning angle (i.e., long optical path) is helpful to get the information of temperature near the surface. The mean DFS is highest at NSA and lowest at TWP. The difference of DFS at 4 km between NSA and TWP is approximately 1.1 at zenith-only and 1.3 at zenith + 10°. This implies that information content for temperature is dependent on climate conditions. Figure 4.2 shows the vertical structure of the fractional DFS defined as:

$$DFS_{fractional} = \frac{DFS_z}{DFS_{4km}} \quad (4.1)$$

Most of the DFS is confined to the lowest levels of the troposphere. At SGP and NSA, 90% of DFS for temperature is found below 1.5 km. At TWP, most of information is below 1 km. This means that AERI is optimized to observe temperature profile especially at lower of troposphere.

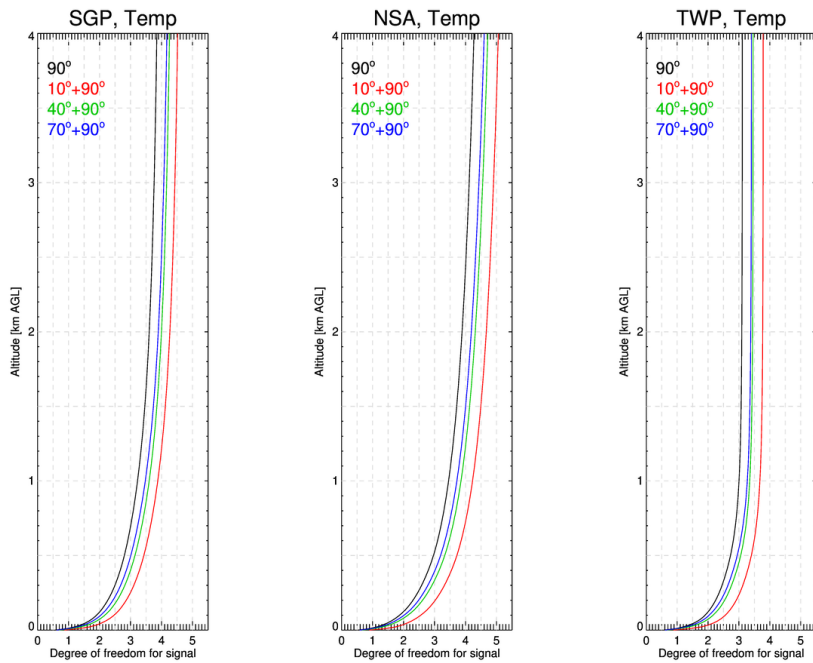


Figure 4.1 Vertical structure of degree of freedom for signal for temperature retrieved from the SGP (left), NSA (middle), and TWP (right) of two scanning angles; 90° (Black), 10° + 90° (red), 40° + 90° (green), 70° + 90° (blue)

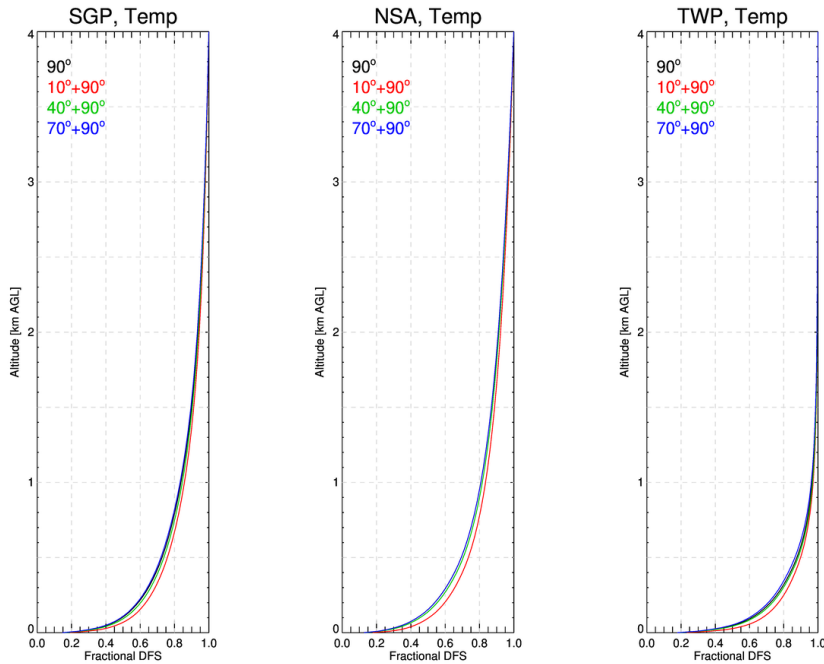


Figure 4.2 Fractional degree of freedom for signal for temperature retrieved from the SGP (left), NSA (middle), and TWP (right) of two scanning angles;  $90^\circ$  (Black),  $10^\circ + 90^\circ$  (red),  $40^\circ + 90^\circ$  (green),  $70^\circ + 90^\circ$  (blue)

Figure 4.3 shows the mean vertical structure of DFS for water vapor of the two scanning angles set. When compared to temperature, additional information of water vapor still exists above 1.5 km at SGP and NSA because the spectral channel used in the AERIOe algorithm for water vapor is less opaque than the one for temperature. The low scanning angle has more information for water vapor only below 200 m. The combination of zenith +  $70^\circ$  result in the largest DFS, and the difference between angles increases with height. The mean DFS is highest at NSA and lowest at TWP. The difference in DFS at 4km between NSA and TWP is approximately 1.8 at zenith-only and 2.1 at zenith +  $70^\circ$ . The

DFS for water vapor is more sensitive to humidity than the DFS for temperature. Figure 4.4 is the vertical structure of the fractional DFS for water vapor. The 90% of DFS for water vapor exists below 3 km at SGP and NSA. TWP has the most of information below 1 km. As a result, DFS for both temperature and water vapor strongly depends on atmospheric humidity. Low scanning angle is helpful to get additional information on temperature near the surface, but it contains only few additional information about water vapor at high altitudes.

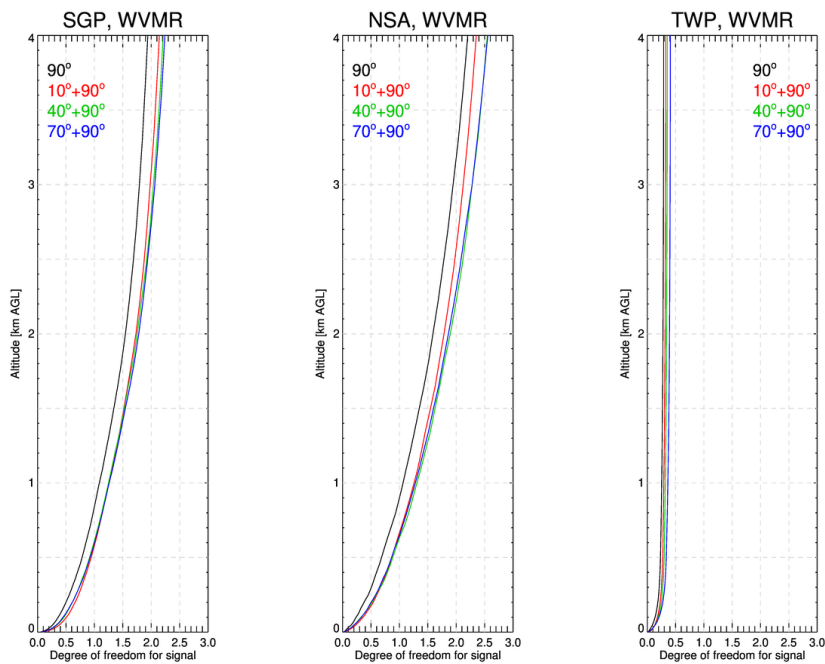


Figure 4.3 Vertical structure of degree of freedom for signal for water vapor retrieved from the SGP (left), NSA (middle), and TWP (right) of two scanning angles; 90° (Black), 10° + 90° (red), 40° + 90° (green), 70° + 90° (blue)

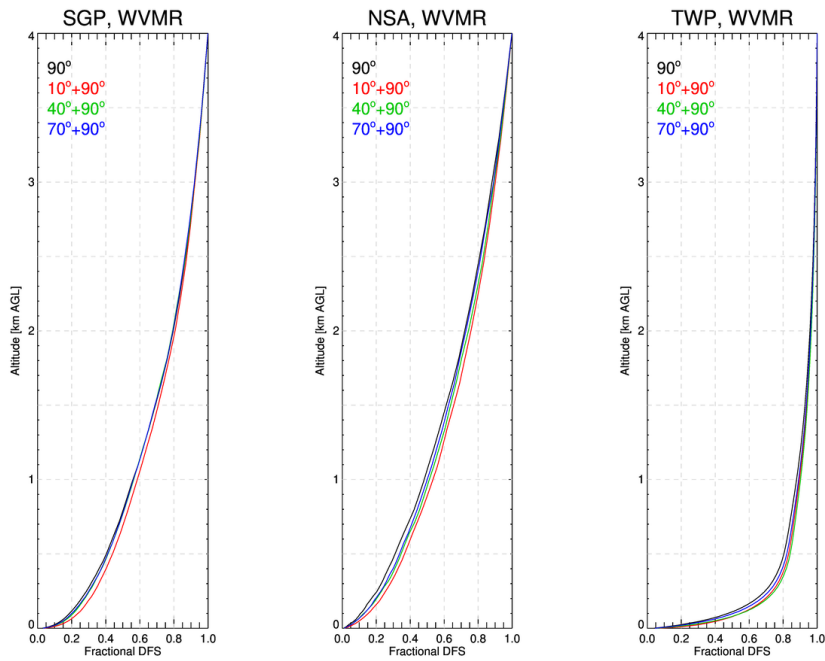


Figure 4.4 Fractional degree of freedom for signal for water vapor retrieved from the SGP (left), NSA (middle), and TWP (right) of two scanning angles;  $90^\circ$  (Black),  $10^\circ + 90^\circ$  (red),  $40^\circ + 90^\circ$  (green),  $70^\circ + 90^\circ$  (blue)

Figures 4.5, 4.6, and 4.7 display the variability of DFS of two scanning angles for temperature and water vapor below 4 km retrieved from radiosonde profiles at the ARM sites. The mean DFS for the temperature of zenith-only is 3.85 (4.27, 3.11) at SGP (NSA, TWP). Zenith with a low scanning angle has more DFS for temperature than zenith with high scanning angle. Zenith with  $10^\circ$  has 17% (18%, 22%) more DFS than zenith-only by an increase of 0.67 (0.79, 0.68) at SGP (NSA, TWP). Also, a zenith with high scanning angle

has the advantage of improving DFS for temperature. Zenith with  $80^\circ$  has 9% (5%, 9%) more DFS than zenith-only by an increase of 0.34(0.23, 0.29) at SGP (NSA, TWP). For the DFS of water vapor, the mean DFS of zenith-only is 1.94 (2.21, 0.29) at SGP (NSA, TWP). Zenith with high scanning angle has a larger DFS than zenith with a low scanning angle, and zenith with  $80^\circ$  has 17% (18%, 46%) more DFS for temperature of Zenith with  $10^\circ$  is 10% (7%, 13%) higher than zenith-only by an increase of 0.20 (0.15, 0.04) at SGP (NSA, TWP). Moreover, the length between the first and third quartile is longer for water vapor than for temperature, which represents that DFS for water vapor is more dependent on atmospheric properties and has higher variability than DFS for temperature. As a result, one additional scanning angle yields approximately 20% more information content in addition to zenith-only. Moreover, near the surface, adding low scanning angle has more benefit of DFS for both temperature and water vapor than adding high scanning angle but it has little additional information of water vapor at high altitude.

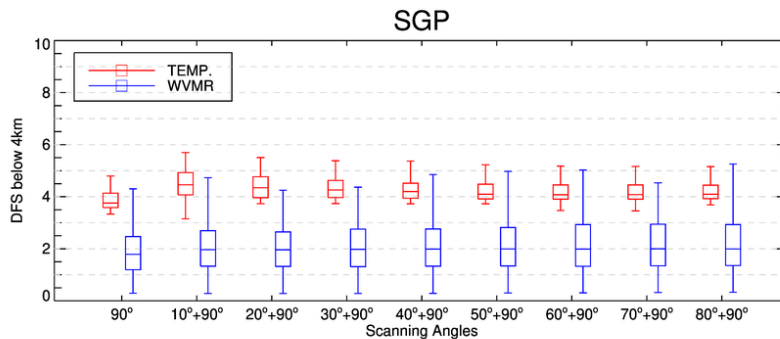


Figure 4.5 Box plot of DFS of two scanning angles for temperature and water vapor below 4 km retrieved from 144 SGP sonde soundings. Box edges are at the first quartile and third quartile, with the median value plotted with a horizontal line.

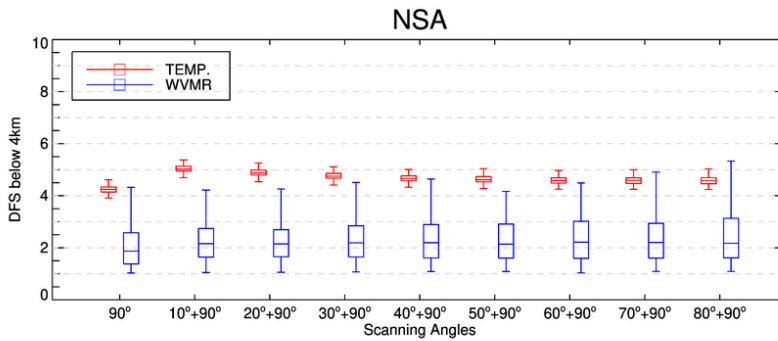


Figure 4.6 Box plot of DFS of two scanning angles for temperature and water vapor below 4 km retrieved from 144 NSA sonde soundings. Box edges are at the first quartile and third quartile, with the median value plotted with a horizontal line.

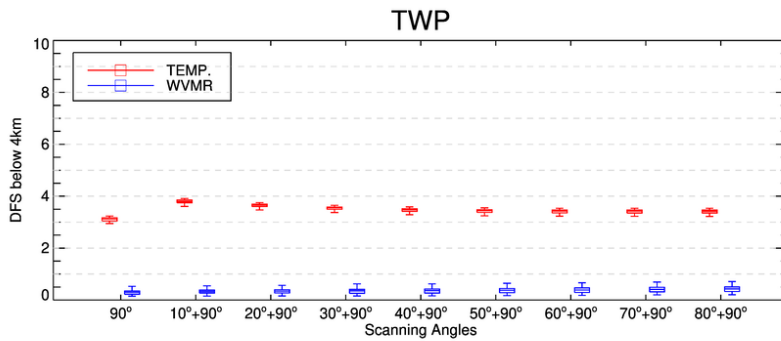


Figure 4.7 Box plot of DFS of two scanning angles for temperature and water vapor below 4 km retrieved from 139 TWP sonde soundings. Box edges are at the first quartile and third quartile, with the median value plotted with a horizontal line.

Figures 4.8, 4.9, and 4.10 show the variability of DFS for multiple scanning angles for temperature and water vapor below 4 km retrieved from radiosonde profiles at the ARM sites. DFS for temperature and water vapor increases with the number of scanning angles. First of all, at DFS for temperature, zenith with four low scanning angles has 28%

(22%, 32%) more DFS than zenith-only by an increase of 1.06 (1.21, 0.99) at SGP (NSA, TWP). Zenith with four low scanning angles and four high scanning angles has 38% (27%, 43%) more DFS than zenith-only by an increase of 1.45 (1.55, 1.33) at SGP (NSA, TWP). Additional four high scanning angles has little impact to DFS for temperature than four low scanning angles. At DFS for water vapor, zenith with four low scanning angles has 30% (30%, 54%) more DFS than zenith-only by an increase of 0.59 (0.67, 0.16) at SGP (NSA, TWP). Zenith with four low scanning angles and four high scanning angles has 59% (74%, 137%) more DFS than zenith-only by an increase of 1.15 (1.63, 0.40) at SGP (NSA, TWP). For water vapor, adding four high scanning angles yields more information than adding four low scanning angles, especially for TWP site where is increased from 54% to 137%. This shows the same results from two scanning angles test: low scanning angle has more information of temperature and high scanning angle has benefit of DFS for water vapor.

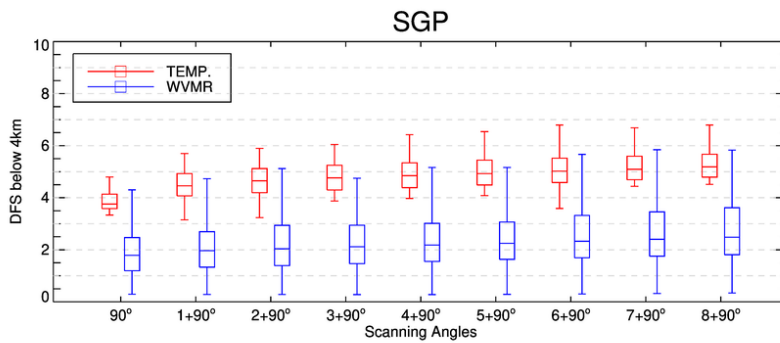


Figure 4.8 Box plot of DFS of multiple scanning angles for temperature and water vapor at 4 km retrieved from 144 SGP sonde soundings. Box edges are at the first quartile and third quartile, with the median value plotted with a horizontal line. (Scanning Angles:  $1+90^\circ = 10^\circ+90^\circ$ ,  $2+90^\circ = 10^\circ+20^\circ+90^\circ$ , ...,  $8+90^\circ = 10^\circ+20^\circ+\dots+70^\circ+80^\circ+90^\circ$ )

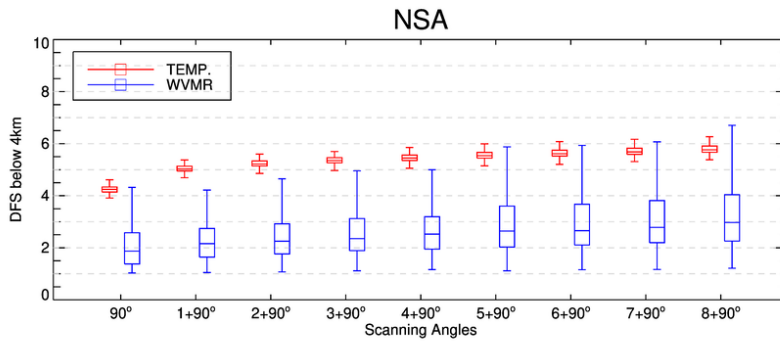


Figure 4.9 Box plot of DFS of multiple scanning angles for temperature and water vapor at 4 km retrieved from 144 NSA sonde soundings. Box edges are at the first quartile and third quartile, with the median value plotted with a horizontal line. (Scanning Angles:  $1+90^\circ = 10^\circ+90^\circ$ ,  $2+90^\circ = 10^\circ+20^\circ+90^\circ$ , ...,  $8+90^\circ = 10^\circ+20^\circ+\dots+70^\circ+80^\circ+90^\circ$ )

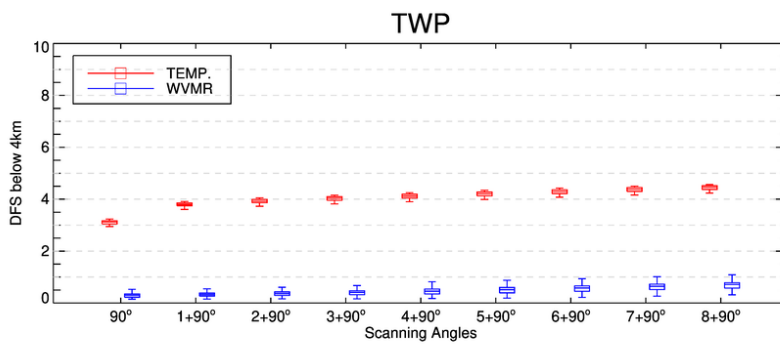


Figure 4.10 Box plot of DFS of multiple scanning angles for temperature and water vapor at 4 km retrieved from 139 TWP sonde. Box edges are at the first quartile and third quartile, with the median value plotted with a horizontal line. (Scanning Angles:  $1+90^\circ = 10^\circ+90^\circ$ ,  $2+90^\circ = 10^\circ+20^\circ+90^\circ$ , ...,  $8+90^\circ = 10^\circ+20^\circ+\dots+70^\circ+80^\circ+90^\circ$ )

## 4.2 Synthetic Experiment – Thermodynamic retrievals

Figure 4.11 shows the root mean square error (RMSE) for temperature (K) of two scanning angles. RMSE is calculated as

$$RMSE_z = \sqrt{\frac{\sum_i^N [a_i(z) - s_i(z)]^2}{N}} \quad (4.2)$$

where  $z$  is altitude and  $N$  is the number of profiles. We define  $a_i(z)$  and  $s_i(z)$  to be either the temperature or water vapor mixing ratio retrieved profile and radiosonde observation respectively. From the zenith-only retrievals, it can be determined that the AERI is typically within 3 K (1.5 K, 0.8 K) of the radiosonde measurement in the lowest 2 km of the atmosphere at SGP (NSA, TWP) with high accuracy near the surface. In contrast to results of DFS for temperature, zenith + 10° shows minor improvement only below 200m, and worse results above 200m. Moreover, adding 70° provides little impact to temperature retrievals compared to zenith-only. The effect of additional angular information is minimal for the temperature retrieval at TWP compared to SGP and NSA. Compared to information content, only one additional scanning angle with zenith has little impact to temperature retrievals except for the bottom of atmosphere.

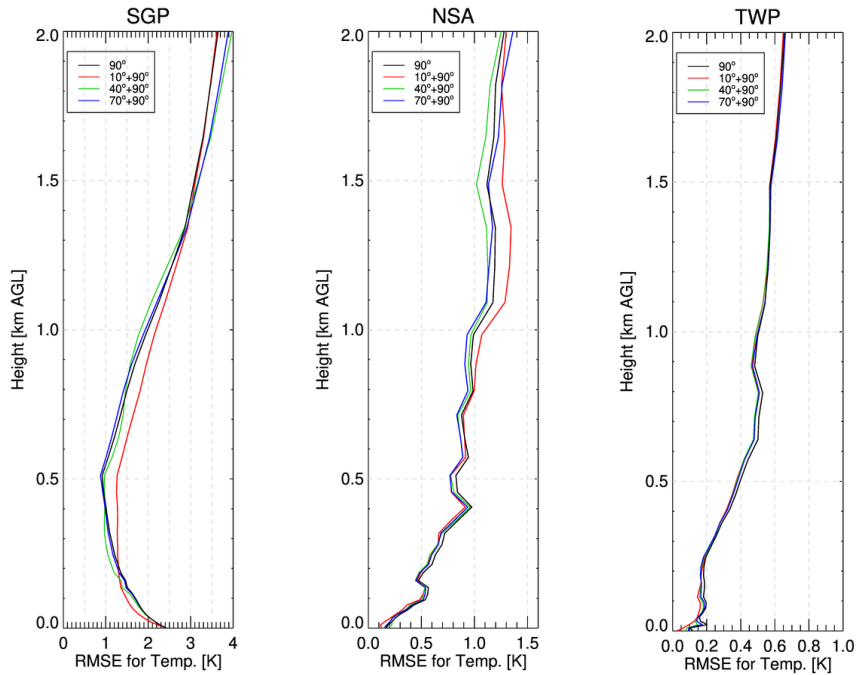


Figure 4.11 AERIOe root mean square error (RMSE) calculations for temperature (K) for the SGP (left), NSA (middle), and TWP (right) synthetic experiment at two scanning angles: 90°(black), 10°+90°(red), 40°+90°(green), and 70°+90°(blue)

Figure 4.12 shows the RMSE for water vapor mixing ratio ( $\text{g kg}^{-1}$ ) of two scanning angles. Water vapor mixing ratio retrieved from AERI radiance is generally within  $2.0 \text{ g kg}^{-1}$  ( $0.6 \text{ g kg}^{-1}$ ,  $1.5 \text{ g kg}^{-1}$ ) of the radiosonde up to 2 km at SGP (NSA, TWP). Within the lowest  $\sim 700 \text{ m}$  of the atmosphere, zenith +  $10^\circ$  performs 30% better in terms of RMSE than the zenith-only by a decrease of  $0.4 \text{ g kg}^{-1}$  at SGP and  $0.1 \text{ g kg}^{-1}$  at NSA. Like temperature retrievals, adding  $70^\circ$  provides little impact to water vapor retrievals compared with zenith-only. As the temperature retrievals, the effect of additional angular

information is weak at TWP. Different from temperature retrievals, one additional scanning angle with zenith, especially low scanning angle, has improvement to water vapor retrievals at SGP and NSA.

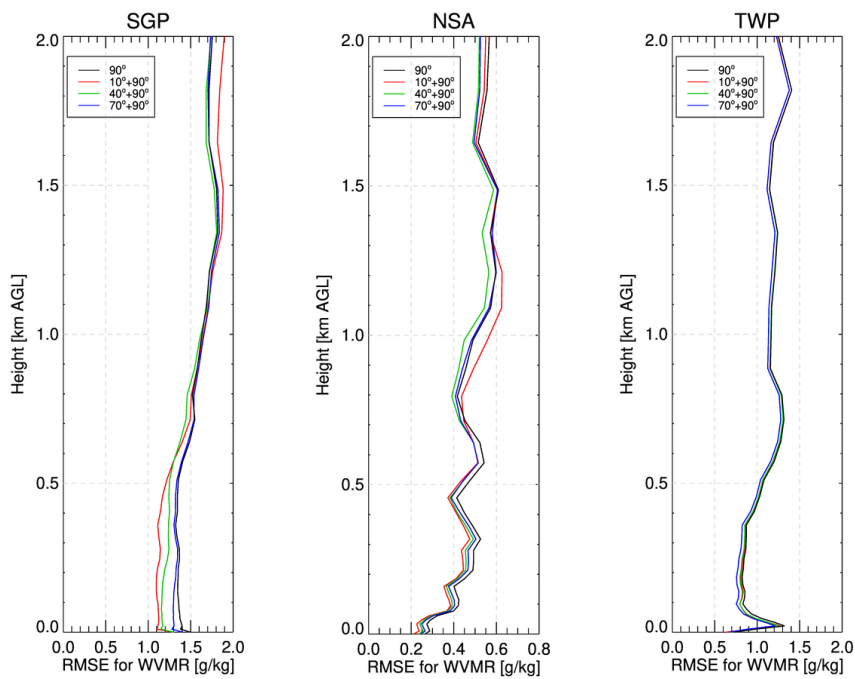


Figure 4.12 AERIoe root mean square error (RMSE) calculations for water vapor mixing ratio ( $g\ kg^{-1}$ ) for the SGP (left), NSA (middle), and TWP (right) synthetic experiment at two scanning angles:  $90^\circ$ (black),  $10^\circ+90^\circ$ (red),  $40^\circ+90^\circ$ (green), and  $70^\circ+90^\circ$ (blue)

Figure 4.13 shows the RMSE for temperature (K) for multiple scanning angles. Zenith with four low scanning angles ( $4+90^\circ$ ) performs better than zenith-only and zenith with  $10^\circ$  ( $1+90^\circ$ ) within the lowest 1200 m at SGP, 1500 m at NSA, and 900 m at TWP.

Zenith with four low scanning angles and four high scanning angles (8+90°) has a similar RMSE profile with zenith with four low scanning angles. This means that additional four high angular information has little advantage in retrieving temperature. This is the same result from DFS for temperature. Figure 4.14 shows the RMSE for water vapor mixing ratio ( $\text{g kg}^{-1}$ ) for multiple scanning angles. Zenith with four low scanning angles performs better than zenith-only and zenith with 10° within the lowest 800 m at SGP, 1500 m at NSA. As for both temperature and water vapor retrievals, including the four low scanning angles and four high scanning angles have no discernible impact on RMSE over the four low scanning alone at SGP and NSA. In contrast, additional high angular information performs better in retrieving water vapor mixing ratio at TWP. This is because the spectral channel used to retrieve water vapor is very opaque at a low scanning angle under humid conditions. A high scanning angle can contain more information about water vapor than a low scanning angle as it is less easily saturated in high humidity conditions, so thermodynamic retrievals can be improved under those conditions when a high elevation angle is included.

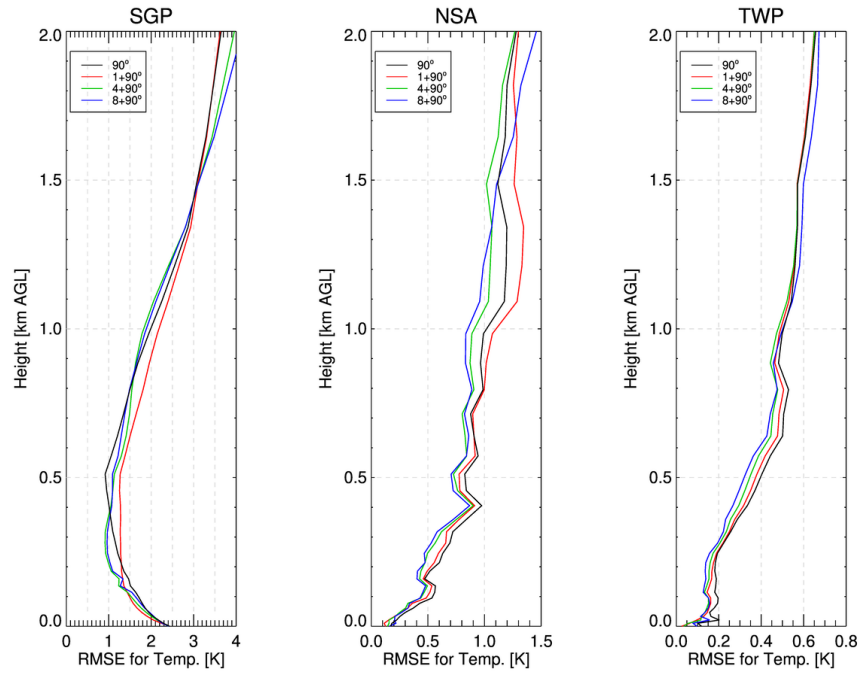


Figure 4.13 AERIOe root mean square error (RMSE) calculations for temperature (K) for the SGP (left), NSA (middle), and TWP (right) synthetic experiment at multiple scanning angles:  $90^\circ$  (black),  $10^\circ + 90^\circ$  (red),  $10^\circ + 20^\circ + 30^\circ + 40^\circ + 90^\circ$  (green), and  $10^\circ + 20^\circ + 30^\circ + 40^\circ + 50^\circ + 60^\circ + 70^\circ + 80^\circ + 90^\circ$  (blue)

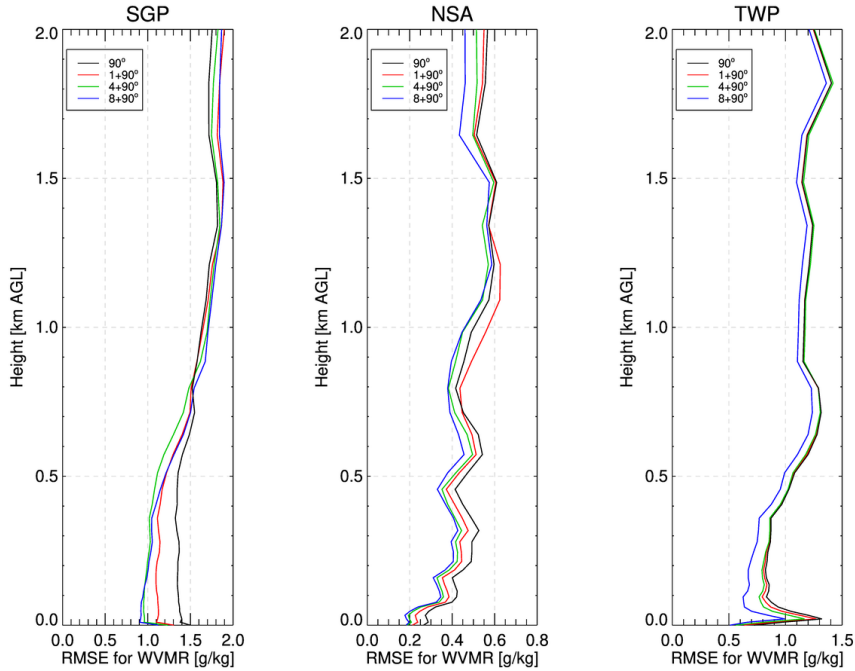


Figure 4.14 AERIoe root mean square error (RMSE) calculations for water vapor mixing ratio ( $g\ kg^{-1}$ ) for the SGP (left), NSA (middle), and TWP (right) synthetic experiment at multiple scanning angles:  $90^\circ$  (black),  $10^\circ+90^\circ$  (red),  $10^\circ+20^\circ+30^\circ+40^\circ+90^\circ$  (green), and  $10^\circ+20^\circ+30^\circ+40^\circ+50^\circ+60^\circ+70^\circ+80^\circ+90^\circ$  (blue)

### 4.3 ACAPEX Campaign – Information Content

Figures 4.15 shows the variability of DFS for two scanning angles for temperature and water vapor below 4 km retrieved from AERI-observed radiances during the ACAPEX campaign. The mean DFS of zenith-only for temperature is 6.67 and for water vapor is 2.61. The mean DFS for temperature is greatest at zenith +  $20^\circ$  which has 7% more than zenith-only by an increase of 0.49. The zenith +  $35^\circ$  has 5% more DFS for temperature

than zenith-only by an increase of 0.36. The zenith + 35° has the largest DFS for water vapor which has 12% more than zenith-only by an increase of 0.32. The zenith + 20° has 9% more than zenith-only by an increase of 0.24. This real-world dataset helps confirm the results of the synthetic experiment shown earlier: that adding 20° has more DFS for temperature than adding 35°, and adding 35° scanning angles has benefit of DFS for water vapor than adding 20°.

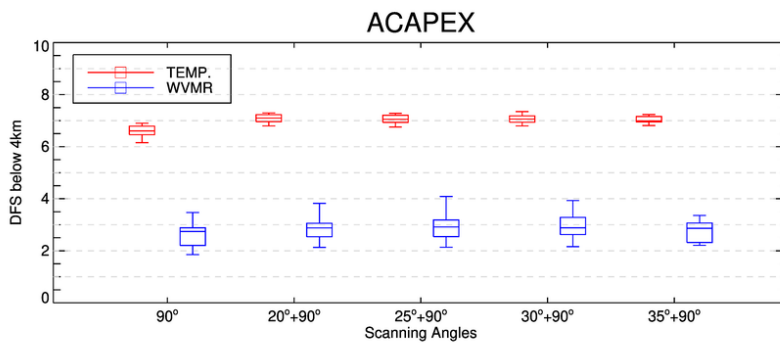


Figure 4.15 Box plot of DFS for temperature and water vapor at 4 km for the ACAPEX campaign at two scanning angles.

Figure 4.16 shows the variability of DFS of multiple scanning angles for temperature and water vapor at 4 km retrieved from AERI-observed radiances during the ACAPEX campaign. The mean DFS for temperature is highest at zenith with four scanning angles (4+90°), which has 13% more DFS than zenith-only by an increase of 0.83. At DFS for water vapor, additional angular information improves. Zenith with four scanning angles has 19% more DFS than zenith-only by an increase of 0.50. Adding more scanning angles indeed has more DFS for both temperature and water vapor. This again

shows that are qualitatively similar to the results from the synthetic experiment as DFS increases for both temperature and water vapor.

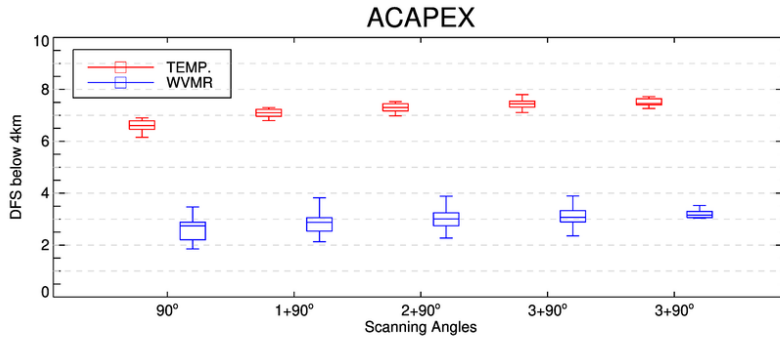


Figure 4.16 Box plot of DFS for temperature and water vapor at 4 km for the ACAPEX campaign at multiple scanning angles. (1 = 90°, 2 = 20°+90°, ...)

#### 4.4 ACAPEX Campaign – Thermodynamic retrievals

Figure 4.17 shows the RMSE for temperature (K) and water vapor mixing ratio ( $\text{g kg}^{-1}$ ) retrieved from AERI-observed radiances during the ACAPEX campaign for two scanning angles. The temperature retrieved from AERI radiances observed at the zenith view is within 1 K below 1 km and 1.5 K above 1 km of the radiosonde measurement. Adding a low scanning angle in general shows an improvement over the zenith-only observation. Zenith + 35° shows the best RMSE, and it has 30% better RMSE than zenith-only with a reduction of 0.2 K below 800 m and 0.4 K above 1500 m. Water vapor mixing ratio retrieved from AERI radiances observed at the zenith view is typically within 1.0  $\text{g kg}^{-1}$  near the surface and 1.5  $\text{g kg}^{-1}$  above 500 m of the radiosonde measurement. Additional angular information improves the retrievals below 1000 m. Zenith + 20°

performs best with a 40% better RMSE than zenith-only by a decrease of  $0.3 \text{ g kg}^{-1}$ . These results are again qualitatively similar to the synthetic experiment.

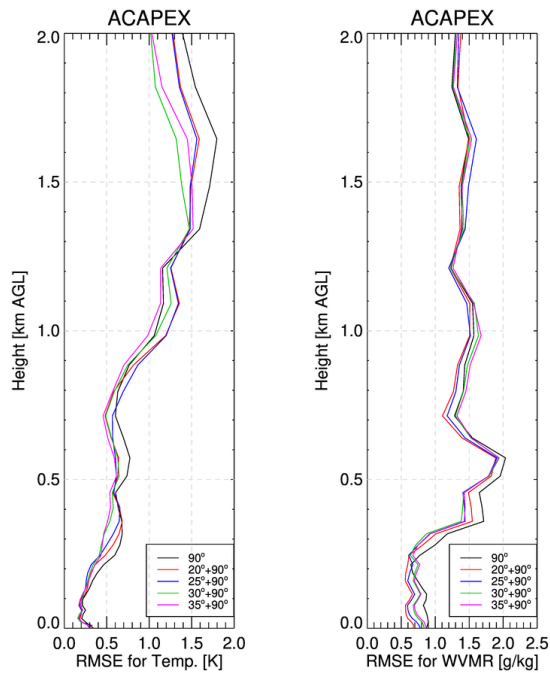


Figure 4.17 AERIoe root mean square error (RMSE) calculations for temperature (K, left) water vapor mixing ratio ( $\text{g kg}^{-1}$ , right) at two scanning angles:  $90^\circ$ (black),  $20^\circ+90^\circ$ (red),  $25^\circ+90^\circ$ (blue),  $30^\circ+90^\circ$ (green), and  $35^\circ+90^\circ$ (magenta)

Figure 4.18 shows the RMSE for temperature (K) and water vapor mixing ratio ( $\text{g kg}^{-1}$ ) retrieved from AERI-observed radiances during the ACAPEX campaign for multiple scanning angles. Zenith with four scanning angles has better RMSE for temperature than zenith-only. Zenith with four scanning angles is within 0.5 K near the

surface and 1 K at 2000 m of the radiosonde measurement. These results show improvement in temperature retrieval performance compared to what was shown in Turner and Lohnert (2014). Zenith + 20° shows the largest improvement in retrieving a water vapor mixing ratio below 1000 m compared to RMSE from zenith-only as well as zenith with additional angles. Zenith + 20° is within 0.5 g kg<sup>-1</sup> near the surface and 1.2 g kg<sup>-1</sup> above 500 m of the radiosonde measurement. The additional angular information improves the water vapor retrievals, especially below 500 m compared to that was in Turner and Lohnert (2014). However, multiple scanning angles shows degraded RMSE for water vapor mixing ratio when compared to the zenith + 20°.

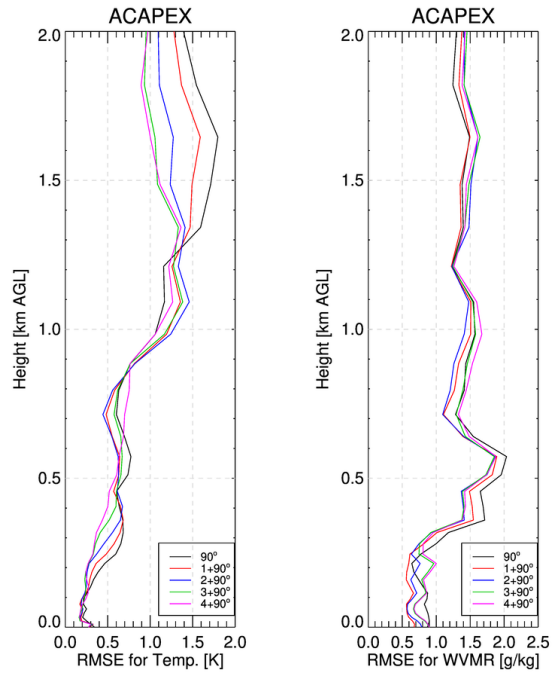


Figure 4. 18 AERIOe root mean square error (RMSE) calculations for temperature (K, left) water vapor mixing ratio ( $g\ kg^{-1}$ , right) at multiple scanning angles: 90°(black), 20 ° +90 ° (red), 20 ° +25 ° +90 ° (blue), 20 ° +25 ° + 30 ° +90 ° (green), and 20°+25° +30°+35°+90°(magenta)

## 5. Conclusions and Future Work

### 5.1 Conclusions

In this study, we investigate using non-zenith scanning angles to improve AERI thermodynamic retrievals and DFS. We have simulated radiances using LBLRTM and radiosondes from the three fixed ARM sites for different climate conditions and AERI observations during the ACAPEX campaign. Clear sky and horizontal homogeneity of the atmosphere are assumed in this study. Two different scanning angle tests have been conducted to study characteristics of scanning angle and effects of numbers of scanning angles.

The results of synthetic experiments have shown that DFS for temperature and water vapor depends on the climate conditions. DFS at the NSA, where water vapor mixing ratio is low, is higher than DFS at the TWP, where it is typically humid. Additional angular information has the benefit of improving DFS for both temperature and water vapor. A low scanning angle has more DFS for temperature than high scanning angle due to the strong absorption of carbon dioxide near the surface. In contrast, high scanning angle provides more information about water vapor at high altitude because the water vapor absorption lines used in the retrievals are more transparent. Zenith with four low scanning angles and four high scanning angles has approximately 40% more DFS for

temperature and 60% more DFS for water vapor than zenith-only retrieved using simulated radiances at ARM sites. During the ACAPEX campaign, the DFSs show consistent results of angular characteristics from synthetic experiments. Zenith with four scanning angles has 13% more DFS for temperature and 20% more DFS for water vapor retrieved using AERI-observed radiance during the ACAPEX campaign.

For the thermodynamic retrievals of the synthetic data, in general adding one high scanning angle has no observable benefit for temperature, though adding one low scanning angle improves the water vapor retrievals. The effect of additional angular information is minimal at the TWP site. Multiple scanning angles have better RMSE than zenith-only below 1 km at all sites. Zenith with four low scanning angles and four high scanning angles shows similar RMSE profiles for temperature and water vapor mixing ratio with zenith with four low scanning angles at the SGP and the NSA. However, at the TWP, additional four high scanning angles have better performance to improve the thermodynamic retrievals. As results from thermodynamic retrievals at synthetic experiment, adding low scanning angles with zenith will be beneficial for future instrument design than adding high scanning angles, and, at least, four low scanning angles will be needed to improve temperature and water vapor retrievals compared to the additional single low scanning angle. In contrast, at location where is consistently humid, adding high scanning angles with zenith will be more useful to improve AERI thermodynamic retrievals than additional low scanning angles.

For the thermodynamic retrievals during the ACAPEX campaign, zenith + 35° shows improvements in retrieving temperature and zenith + 20° has better RMSE for water vapor mixing ratio than zenith-only and zenith with other scanning angles.

Moreover, the zenith with four low scanning angles improves the AERI temperature retrievals. The zenith with four low scanning angles is within 0.5 K below 1 km and 1.0 K at 2 km of the radiosondes. In contrast, the zenith + 20° shows better RMSE for water vapor than the zenith with four scanning angles. It might be because the variability of water vapor mixing ratio within time difference is high over the ocean. Additionally, the assumption for water vapor to be horizontally homogenous is sometimes invalid (Massaro et al., 2015). So, we need more case studies to verify the improvement of AERI thermodynamic retrievals using multiple scanning angles for the future.

## 5.2 Future Work

Due to the limitations of ACAPEX campaign, only 62 observed profiles in 3 days were able to be used in this study. So, first possible future work includes examining using multiple scanning angles to improve AERI thermodynamic retrievals using observations from the Multidisciplinary Drifting Observatory for the Study of Arctic Climate (MOSAIC) campaign between 11 October 2019 and 31 October 2020 which has longer observing periods than ACAPEX campaign. MOSAIC was aimed to study arctic climate change which is amplified relative to global change and is embodied by a dramatic decline in the perennial sea-ice pack. The same M-AERI instrument as in ACAPEX was also deployed during MOSAIC and scanned the atmosphere at multiple elevation angles. The longer length of the campaign should allow for more clear-sky observations to be used in a more comprehensive case study of multiple scanning angles.

In this study, the spectral channels we used in the algorithm are identical at all scanning angles. However, Crewell and Löhnert (2007) had found that the best performance throughout the troposphere was achieved when the four most opaque frequencies were used with additional angular information and the three more transparent channels were added with zenith-only in MWR retrievals. Moreover, from synthetic experiment, the results of multiple scanning angles are different between NSA and TWP sites: low scanning angle is more useful to improve AERI retrievals at NSA, but high scanning angle has more benefit of improvement of retrievals at TWP due to the consistent humid conditions which make the spectral channels become opaque near the surface. For the locations which are consistently humid, using more transparent channel and high scanning angles could help get additional information and accuracy of retrievals. Therefore, we can find multi-spectral channels to improve the AERI retrievals with multiple scanning angles depending on the different climate conditions.

This study was also limited to clear sky even though the AERIOe algorithm is capable of retrieving thermodynamic profiles in both clear and cloudy conditions up to the cloud base height. Additionally, the assumption of horizontal homogeneity of the atmosphere is more valid under the stratiform clouds (Petty 2006). Moreover, the clouds are very opaque for the IR band, so a low scanning angle can have benefits of retrieving cloud properties. As a result, it may be valuable to use multiple scanning angles to improve AERI thermodynamic retrievals under the cloudy conditions.

## Reference

- August, T., D. Klaes, P. Schlüssel, T. Hultberg, M. Crapeau, A. Arriaga, A. O'Carroll, D. Coppens, R. Munro, and X. Calbet, 2012: IASI on Metop-A: Operational level 2 retrievals after five years in orbit. *Journal of Quantitative Spectroscopy & Radiative Transfer*, **113**, 1340-1371.
- Aumann, H.H., M.T. Chahine, C. Gautier, M. Goldberg, E. Kalnay, L. Mcmillin, H. Revercomb, P.W. Rosenkranz, W. L. Smith, D. Staelin, L. Strow, and J. Susskind, 2003: AIRS/AMSU/HSB on the Aqua mission: design, science objectives, data, products, and processing systems. *IEEE Transactions on Geoscience and Remote Sensing*, **41**, 253-264, doi: 1109/TGRS.2002.808356.
- Cadeddu, M. P., J. C. Liljegren, and D. D. Turner, 2013: The Atmospheric radiation measurement (ARM) program network of microwave radiometers: instrumentation, data, and retrievals. *Atmos. Meas. Tech.*, **6**, 2359-2372.
- Cayla, FR., 1993: IASI Infrared Interferometer for Operations and Research. In *High Spectral Resolution Infrared Remote Sensing for Earth's Weather and Climate Studies. NATO ASI*, **19**, Edited by A. Chédin, M. T. Chahine, and N. A. Scott, 9-19, Springer, Berlin, Heidelberg. doi: [10.1007/978-3-642-84599-4\\_2](https://doi.org/10.1007/978-3-642-84599-4_2).
- Chédin, A., M. T. Chahine, and N. A. Scott (Eds), 1993: High Spectral Resolution Infrared Remote Sensing for Earth's Weather and Climate Studies, *NATO ASI Ser.*, **19**, Springer, Berlin.

- Cimini, D., O. Caumont, U. Löhnert, L. Alados-Arboledas, R. Bleisch, J. Fernandez-Galvez, T. Huet, M. E. Ferrario, F. Madonna, O. Maier, F. Nasir, G. Pace, and R. Posada, 2012: An international network of ground-based microwave radiometers for the assimilation of temperature and humidity profiles into NWP model. 9th International Symposium on Tropospheric Profiling (ISTP). L'Aquila, Italy, Abstract 45, 3-7 Sept.
- Clough, S. A., M.W. Shephard, E. J. Mlawer, J. S. Delamere, M. J. Iacono, K. Cady-Pereira, S. Boukabara, and P. D. Brown, 2005: Atmospheric radiative transfer modeling: a summary of the AER codes. *Journal of Quantitative Spectroscopy & Radiative Transfer*, **91**, 233-244.
- Crewell, S., H. Bloemin, A. Feijt, S. G. Garcia, D. Jolivet, O. A. Krasnov, A. van Lammeren, U. Löhnert, E. van Meijgaard, J. Meywerk, M. Quante, K. Pfeilsticker, S. Schmidt, T. Scholl, C. Simmer, M. Schroder, T. Trautmann, V. Venema, M. Wendisch, and U. Willen, 2004: The BALTEX Bridge Campaign: An integrated approach for a better understanding of clouds. *Bull. Am. Meteorol. Soc.*, **124**, 1767-1785.
- Crewell, S., and U. Löhnert, 2007: Accuracy of Boundary Layer Temperature Profiles Retrieved with Multifrequency Multiangle Microwave Radiometry. *IEEE Transactions on Geoscience and Remote Sensing*, **45**, 2195-2201, doi: 10.1109/TGRS.2006.888.434.
- Del Genio, A. D., and A. B. Wolf, 2000: The temperature dependence of the liquid water path of low clouds in the southern great plains. *J. Clim.*, **13**, 3465-3486.
- Dimitrova, R., Z. Silber, T. Zsedrovits, C. M. Hocut, L. S. Leo, S. D. Sabatino, and H. J. S. Fernando, 2016: Assessment of Planetary Boundary-Layer Schemes in the weather research and forecasting mesoscale model using MATERHORN field data. *Boundary-Layer Meteorol.*, **159**, 589-609.

- Doran J. C., S. Zhong, J. C. Liljegren, and C. Jakob, 2002: A comparison of cloud properties at a coastal and inland site at the North Slope of Alaska. *J. Geophys. Res.*, **107**, D11, 4120, doi: 10.1029/2001JD000819.
- Durre, I., and X. Yin, 2008: Enhanced radiosonde data for studies of vertical structure. *Bull. Am. Meteorol. Soc.*, **89**, 1257-1262.
- Ebell, K., E. Orlandi, A. Hunerbein, U. Löhnert, and S. Crewell, 2013: Combining ground-based with satellite-based measurements in the atmospheric state retrieval: Assessment of the information content. *J. Geophys. Res. Atmos.*, **118**, 6940-6956.
- Esau, I. and S. Zilitinkevich, 2010: On the role of the planetary boundary layer depth in the climate system. *Adv. Sci. Res.*, **4**, 63-69.
- Fairall, C. W., S. Y. Matrosov, C. R. Williams, and E. J. Walsh, 2018: Estimation of Rain Rate from Airborne Doppler W-Band Radar in CalWater-2. *J. Atmos. Ocean. Technol.*, **35**, 593-608, doi: 10.1175/JTECH-D-17-0025.1.
- Feltz, W. F., W. L. Smith, R. O. Knuteson, H. E. Revercomb, H. M. Woolf, and H. B. Howell, 1998: Meteorological applications of temperature and water vapor retrievals from the ground-based Atmospheric Emitted Radiance Interferometer (AERI). *J. Appl. Meteorol.*, **37**, 857-875.
- Feltz, W. F., W. L. Smith, H. B. Howell, R. O. Knuteson, H. Woolf, and H. E. Revercomb, 2003: Near continuous profiling of temperature, moisture, and atmospheric stability using the Atmospheric Emitted Radiance Interferometer (AERI). *J. Appl. Meteorol.*, **42**, 584-597.
- Gero, P. J., and D. D. Turner, 2011: Long-Term Trends in Downwelling Spectral Infrared Radiance over the U.S. Southern Great Plains. *J. Clim.* **24**, 4831-4843, doi: 10.1175/2011JCLI14210.1.

- Gero, P. J., R. Knuteson, D. Hackel, F. Best, R. Garcia, C. Phillips, H. Revercomb, W. Smith, E. Verret, S. Lantagne, and C. Roy, 2015: A new marine atmospheric emitted radiance interferometer for shipboard atmospheric and oceanic observations. In Fourier Transform Spectroscopy and Hyperspectral Imaging and Sounding of the Environment, OSA Technical Digest (online) (Optical Society of America), paper JM1A.2.
- Han, Y., H. Revercomb, M. Crompton, D. Gu, D. Johnson, D. Mooney, D. Scott, L. Strow, G. Bingham, L. Borg, Y. Chen, D. DeSloover, M. Esplin, D. Hagan, X. Jin, R. Knuteson, H. Motteler, J. Predina, L. Suwinski, J. Taylor, D. Tobin, D. Tremblay, C. Wang, L. Wang, and V. Zavyalov, 2013: Suomi NPP CrIS measurements, sensor data record algorithm, calibration and validation activities, and record data quality. *J. Geophys. Res. Atmos.*, **118**, 12,734-12,748, doi: 10.1002/2013JD020344.
- Higgins, R. W., J. -K. E. Schemm, W. Shi, and A. Leetmaa, 2000: Extreme Precipitation Events in the Western United States Related to Tropical Forcing. *J. Climate*, **13**, 793-820.
- Hilton, F. I., S. M. Newman, and A.D. Collard, 2012: Identification of NWP humidity biases using high-peaking water vapour channels from IASI. *Atmos. Sci. Lett.*, **13**, 73-78, doi: 10.1002/asl.366.
- Huang, H. L., W. L. Smith, and H. M. Woolf, 1992: Vertical resolution and accuracy of atmospheric infrared sounding spectrometers. *Bull. Am. Meteorol. Soc.*, **93**, 347-370, doi:10.1175/BAMS-D-11-00027.1.
- Knuteson, R. O., H. E. Revercomb, F. A. Best, N. C. Ciganovich, R. G. Dedecker, T. P. Dirks, S. C. Ellington, W. F. Feltz, R. K. Garcia, H. B. Howell, W. L. Smith, J. F. Short, and D. C. Tobin, 2004a: Atmospheric Emitted Radiance Interferometer. Part I: Instrument Design. *J. Atmos. Oceanic Technol.*, **21**, 1763-1766, doi: 10.1175/JTECH-1662.1.

- Knuteson, R. O., H. E. Revercomb, F. A. Best, N. C. Ciganovich, R. G. Dedecker, T. P. Dirks, S. C. Ellington, W. F. Feltz, R. K. Garcia, H. B. Howell, W. L. Smith, J. F. Short, and D. C. Tobin, 2004b: Atmospheric Emitted Radiance Interferometer. Part II: Instrument Performance. *J. Atmos. Oceanic Technol.*, **21**, 1777-1789, doi: 10.1175/JTECH-1663.1.
- Li, J., W. W. Wolf, W. P. Menzel, W. Zhang, H. L. Huang, and T. H. Achtor, 2000: Global Soundings of the Atmosphere from ATOVS Measurements: The Algorithm and Validation. *J. Appl. Meteorol.*, **39**, 1248-1268.
- Liljegren, J. C., 2004: Improved retrievals of temperature and water vapor profiles with a twelve-channel radiometer. Eighth Symposium on Integrated Observing and Assimilation Systems for Atmosphere, Oceans, and Land Surface (IOAS-AOLS), *Am. Meteorol. Soc.*, Seattle, Washington, 11-15 Jan.
- Löhnert, U., and S. Crewell, 2003: Accuracy of cloud liquid water path from ground-based microwave radiometry: 1. Dependency on cloud model statistics. *Radio Science*, **38**, 8041-8051.
- Löhnert, U., S. Crewell, and C. Simmer, 2004: An Integrated approach toward retrieving physically consistent profiles of temperature, humidity, and cloud liquid water, *J. Appl. Meteorol.*, **43**, 1295-1307.
- Massaro, G., C. Serio, and P. Antonelli, 2012: Inversion for atmospheric thermodynamical parameters of IASI data in the principal components space. *Q. J. R. Meteorol. Soc.*, **138**, 103-117, doi: 10.1002/qj.909.
- Massaro, G., I. Stiperski, B. Pospichal, and M. W. Rotach, 2015: Accuracy of retrieving temperature and humidity profiles by ground-based microwave radiometry in truly complex terrain. *Atmos. Meas. Tech.*, **8**, 3355-3367.

- Matthias, V., and J. Bøsenberg, 2002: Aerosol climatology for the planetary boundary layer derived from regular lidar measurements. *Atmos. Res.*, **63**, 221-245.
- Miao Yucong, and Liu Shuhua, 2019: Linkages between aerosol pollution and planetary boundary layer structure in China. *Science of the Total Environment*, **650**, 288-296.
- Minnett P. J., R. O. Knuteson, F. A. Best, B. J. Osborne, J. A. Hanafin, and O. B. Brown, 2000: The Marine-Atmospheric Emitted Radiance Interferometer: A High-Accuracy, Seagoing Infrared Spectrometer. *J. Atmos. Ocean. Technol.*, **18**, 994-1013.
- National Academies of Sciences, Engineering, and Medicine., 2018: Thriving on Our Changing Planet: A Decadal Strategy for Earth Observation from space. Washington, DC: The National Academies Press. doi: 10.17226/24938.
- National Research Council (NRC), 2009: Committee on developing mesoscale meteorological observational capabilities to meet multiple national needs, in *Observing Weather and Climate From the Ground Up: A Nationwide Network of Networks*. Washington, DC, USA: National Academies Press, 234pp.
- Pan, HL., and L. Mahrt, 1987: Interaction between soil hydrology and boundary-layer development. *Boundary-Layer Meteorol.*, **38**, 185-202.
- Petty, G. W., 2006: A First Course in Atmospheric Radiation. 2nd ed. Sundog Publishing, 472 pp.
- Pleim, J. E., and A. Xiu., 1995: Development and testing of a surface flux and planetary boundary layer model for application in mesoscale models. *J. Appl. Meteorol.*, **34**, 16-32.
- Pougatchev, N., T. August, X. Calbet, T. Hultberg, O. Oduleye, P. Schlüssel, B. Stiller, K. St. Germain, and G. Bingham, 2009: IASI temperature and water vapor retrievals – error assessment and validation. *Atmos. Chem. Phys.*, **9**, 6453-6458.

- Rodgers C. D., 2000: Inverse Methods for Atmospheric Sounding: Theory and Practice. Series on Atmospheric, Oceanic and Planetary Physics, Vol. 2, World Scientific, 238 pp.
- Rothman L. S., and I. E. Gordon, 2013: The HITRAN Molecular Database. In *Eighth International Conference on Atomic and Molecular Data and their Applications*, **1545**, 223-231, doi: 10.1063/1.4815858
- Rosenfeld, D., and A. Givati, 2006: Evidence of Orographic Precipitation Suppression by Air Pollution-Induced Aerosols in the Western United States. *J. Appl. Meteorol. Climatol*, **45**, 893-911.
- Rutz, J. J., W. J. Steenburgh, and F. M. Ralph, 2014: Climatological characteristics of atmospheric rivers and their inland penetration over the western United States. *Mon. Weather Rev.*, **142**, 905-921.
- Schwalb, A., 1978: The TIROS N/NOAA A-G satellite series. *NOAA Techh. Mem., NESS 95*.
- Smith W. L., W. F. Feltz, R. O. Knuteson, H. E. Revercomb, H. M. Woolf, and H. B. Howell, 1999: The retrieval of planetary boundary layer structure using ground-based infrared spectral radiance measurements. *J. Atmos. Ocean. Technol.*, **16**, 323-333.
- Stephens, G. L., 1994: Remote Sensing of the Lower Atmosphere, *Oxford Univ. Press, Oxford*.
- Stull, R., 2011: Meteorology for Scientists and Engineers. 3rd ed. (Uni. Of British Columbia).
- Susskind J., J. Rosenfield, and D. Reuter, 1984: *J. Geophys. Res.*, **89**, 4677-4697.
- Toporov M., and U. Lohnert, 2020: Synergy of Satellite- and Ground-Based Observations for Continuous Monitoring of Atmospheric Stability, Liquid Water Path, and Integrated Water Vapor: Theoretical Evaluations Using Reanalysis and Neural Networks. *J. Appl. Meteorol. Climatol.* **59**, 1153-1170.

- Turner, D. D., and J. E. M. Goldsmith, 1999: Twenty-four-hour Raman lidar water vapor measurements during the Atmospheric Radiation Measurement Program's 1996 and 1997 water vapor intensive observation periods, *J. Atmos. Oceanic Technol.*, **16**, 1062-1076.
- Turner, D. D., W. F. Feltz, and R. A. Ferrare, 2000: Continuous Water Vapor Profiles from Operational Ground-Based Active and Passive Remote Sensors. *Bull. Amer. Meteor. Soc.*, **81**, 1301-1317.
- Turner, D. D., B. M. Lesht, S. A. Clough, L. C. Liljegren, H. E. Revercomb, and D. C. Tobin, 2003: Dry bias and variability in Vaisala RS80-H radiosondes: The ARM experience, *J. Atmos. Oceanic Technol.*, **20**, 117-132.
- Turner, D. D., D. C. Tobin, S. A. Clough, P. D. Brown, R. G. Ellingson, E. J. Mlawer, R. O. Knuteson, H. E. Revercomb, T. R. Shippert, and W. K. Smith, 2004: The QME AERI LBLRTM: A closure experiment for downwelling high spectral resolution infrared radiance. *J. Atmos. Sci.*, **61**, 2657-2675, doi:10.1175/JAS3301.1.
- Turner, D. D., 2005: Arctic Mixed-Phase Cloud Properties from AERI Lidar Observations: Algorithm and Results from SHEBA. *J. Appl. Meteorol.*, **44**, 427-444
- Turner, D. D., S. A. Clough, J. C. Liljegren, E. E. Clothiaux, K. E. Cady-Pereira, and K. L. Gaustad, 2007a: Retrieving liquid water path and precipitable water vapor from the atmospheric radiation measurement (ARM) microwave radiometers. *IEEE Transaction on Geoscience and Remote Sensing*, **45**, 3680-3690.
- Turner, D. D., 2007b: Improved ground-based liquid water path retrievals using a combined infrared and microwave approach. *J. Geophys. Res.*, **112**, D15204, doi:10.1029/2007JD008530

- Turner, D. D., 2008: Ground-based infrared retrievals of optical depth, effective radius, and composition of airborne mineral dust above the Sahel. *J. Geophys. Res.*, **113**, D00E03, doi: 10.1029/2008JD010054
- Turner, D. D., and U. Löhnert, 2014: Information content and uncertainties in thermodynamic profiles and liquid cloud properties retrieved from the ground-based atmospheric emitted radiance interferometer (AERI). *J. Appl. Meteorol. Climatol.*, **53**, 752-771, doi:10.1175/JAM-C-D-13-0126.1.
- Turner, D. D., and W. G. Blumberg, 2018: Improvements to the AERIOe Thermodynamic Profile Retrieval Algorithm. *IEEE J. Sel. Top. Appl. Earth Obs. Remote Sens.*, in press. doi: 10.1109/JSTARS\_2018.2874968
- Wagner T. J., W. F. Feltz, and S. A. Ackerman, 2008: The temporal evolution of convective indices in storm-producing environments. *Wea. Forecasting*, **23**, 786-794.
- Wagner T. J., D. D. Turner, L. K. Berg, and S. K. Krueger, 2013: Ground-based remote retrievals of cumulus entrainment rates. *Atmos. Oceanic Techno.*, **30**, 1460-1471.
- Wells R. J., 1999: Rapid approximation to the Voigt/Faddeeva function and its derivatives. *J. Q. Spectrosc. Radiat. Transfer*, **62**, 29-48.
- Wulfmeyer, V., R. M. Hadrdesty, D. D. Turner, A. Behrendt, M. P. Cadeddu, P. Di Girolamo, P. Schlüssel, J. Van Baelen, and F. Zus, 2015: A review of the remote sensing of lower tropospheric thermodynamic profiles and its indispensable role for the understanding and the simulation of water and energy cycles. *Rev. Geophys.*, **53**, 819-895, doi: 10.1002/2014RG000476.
- Yurganov, L., W. McMillan, C. Wilson, M. Fischer, S. Biraud, and C. Sweeney, 2010: Carbon monoxide mixing ratios over Oklahoma between 2002 and 2009 retrieved from

Atmospheric Emitted Radiance Interferometer spectra. *Atmos. Meas. Tech.*, **3**, 1319-1331,  
doi: 10.5194/amt-3-1319-2010

